Kruijssen, JMD, Pfeffer, JL, Reina-Campos, M, Crain, RA and Bastian, N

 The formation and assembly history of the Milky Way revealed by its globular cluster population

http://researchonline.ljmu.ac.uk/id/eprint/11138/

Article

The formation and assembly history of the Milky Way revealed by its globular cluster population

J. M. Diederik Kruijssen [1]*, Joel L. Pfeffer,[2] Marta Reina-Campos,[1] Robert A. Crain [2] and Nate Bastian[2]

[1]*Astronomisches Rechen-Institut, Zentrum für Astronomie der Universität Heidelberg, Mönchhofstraße 12-14, D-69120 Heidelberg, Germany*
[2]*Astrophysics Research Institute, Liverpool John Moores University, IC2, Liverpool Science Park, 146 Brownlow Hill, Liverpool L3 5RF, UK*

ABSTRACT

We use the age–metallicity distribution of 96 Galactic globular clusters (GCs) to infer the formation and assembly history of the Milky Way (MW), culminating in the reconstruction of its merger tree. Based on a quantitative comparison of the Galactic GC population to the 25 cosmological zoom-in simulations of MW-mass galaxies in the E-MOSAICS project, which self-consistently model the formation and evolution of GC populations in a cosmological context, we find that the MW assembled quickly for its mass, reaching $\{25, 50\}$ per cent of its present-day halo mass already at $z = \{3, 1.5\}$ and half of its present-day stellar mass at $z = 1.2$. We reconstruct the MW's merger tree from its GC age–metallicity distribution, inferring the number of mergers as a function of mass ratio and redshift. These statistics place the MW's assembly *rate* among the 72th–94th percentile of the E-MOSAICS galaxies, whereas its *integrated* properties (e.g. number of mergers, halo concentration) match the median of the simulations. We conclude that the MW has experienced no major mergers (mass ratios >1:4) since $z \sim 4$, sharpening previous limits of $z \sim 2$. We identify three massive satellite progenitors and constrain their mass growth and enrichment histories. Two are proposed to correspond to Sagittarius (a few $10^8 \, \mathrm{M_\odot}$) and the GCs formerly associated with Canis Major ($\sim 10^9 \, \mathrm{M_\odot}$). The third satellite has no known associated relic and was likely accreted between $z = 0.6$ and 1.3. We name this enigmatic galaxy *Kraken* and propose that it is the most massive satellite ($M_* \sim 2 \times 10^9 \, \mathrm{M_\odot}$) ever accreted by the MW. We predict that ~ 40 per cent of the Galactic GCs formed *ex situ* (in galaxies with masses $M_* = 2 \times 10^7$–$2 \times 10^9 \, \mathrm{M_\odot}$), with 6 ± 1 being former nuclear clusters.

Key words: Galaxy: evolution – Galaxy: formation – globular clusters: general – Galaxy: halo – Galaxy: stellar content – galaxies: star formation.

1 INTRODUCTION

It has been known for more than half a century that the Milky Way formed through a process of gravitational collapse (Eggen, Lynden-Bell & Sandage 1962). In the decades since, it has become clear that galaxy formation is a continuous hierarchical process, in which central hubs grow through a combination of rapid, *in situ* star formation (dominant at early cosmic times) and the gradual accretion of smaller satellites (in the context of this work, see e.g. Searle & Zinn 1978; White & Rees 1978; White & Frenk 1991; Forbes, Brodie & Grillmair 1997; Côté, Marzke & West 1998; Côté et al. 2000; Oser et al. 2010; Beasley et al. 2018). More recently, deep observations of stellar haloes are revealing the relics of this

ongoing accretion process, during which dwarf galaxies are tidally disrupted and their debris builds up the central galaxy's halo (e.g. Ibata, Gilmore & Irwin 1994; Martin et al. 2004; Belokurov et al. 2006; Grillmair 2009; McConnachie et al. 2009; Crnojević et al. 2016).

While the relics of the galaxy formation and assembly process are now found in haloes throughout the local Universe, a comprehensive picture of the formation and assembly history of the Milky Way is still lacking. The existing constraints on the Galaxy's assembly history are generally based on its most recent accretion events (e.g. Martin et al. 2004; Belokurov et al. 2006) or on indirect inference using comparisons to (cosmological) simulations of galaxy formation and evolution (e.g. Wyse 2001; Stewart et al. 2008; Shen et al. 2010; Deason et al. 2013; Mackereth et al. 2018, Hughes et al. in prep.). These approaches have provided two major insights. Firstly, the hierarchical growth of the Milky Way through satellite accretion is

still continuing at the present day. Secondly, these accretion events predominantly correspond to minor mergers, with the last major merger having taken place at $z > 2$. An extensive body of literature aims to refine these results and obtain a complete understanding of the Galaxy's formation and assembly history (see e.g. Belokurov 2013 for a recent review).

In this paper, we constrain the formation and assembly history of the Milky Way by applying a new technique that combines and expands on previous approaches – we perform a quantitative and detailed comparison to a suite of cosmological zoom-in simulations and use the insights from this comparison to reconstruct the merger tree of the Milky Way. Specifically, we draw inspiration from the seminal paper by Searle & Zinn (1978), who used the Galactic globular cluster (GC) population to infer that the GCs in the Galactic halo formed over a longer timespan than the GCs associated with the Galactic bulge, leading to the conclusion that the Milky Way grew by hierarchical galaxy growth. This idea has since been refined – improved measurements of the ages of GCs have shown that the distribution of Galactic GCs in age–metallicity space is bifurcated (e.g. Marín-Franch et al. 2009), with a young and metal-poor branch tracing part of the GC population thought to result from satellite galaxy accretion (e.g. Forbes & Bridges 2010; Leaman, VandenBerg & Mendel 2013). These results suggest that the detailed age–metallicity distribution of GCs may be used to infer the accretion history of the host galaxy.

The key ingredient enabling us to extract the wide range of information encoded in the Galactic GC population is the E-MOSAICS [1] project (Pfeffer et al. 2018; Kruijssen et al. 2019). Cluster formation and disruption are well known to depend on the local environmental conditions within galaxies (see recent reviews by Kruijssen 2014; Forbes et al. 2018). Modelling the co-formation and co-evolution of GC populations and their host galaxies thus requires following the spatial and kinematic phase-space distributions of the cluster populations self-consistently in their cosmological context. This prohibits the use of models based on semi-analytic or particle tagging techniques. Instead, E-MOSAICS self-consistently couples environmentally dependent sub-grid models for the formation, evolution, and tidal disruption of stellar clusters (MOSAICS, Kruijssen et al. 2011, 2012; Pfeffer et al. 2018) to the locally resolved baryonic conditions obtained with the state-of-the-art cosmological galaxy formation model EAGLE (Schaye et al. 2015; Crain et al. 2015). The initial set of 25 hydrodynamical cosmological zoom-in simulations of Milky Way-mass galaxies allows us to follow the co-formation and co-evolution of galaxies and their GC populations.

Specifically, we show in Kruijssen et al. (2019) that the distribution of GCs in age–metallicity space is a sensitive probe of the host galaxy's formation and assembly history. The GC age–metallicity distributions obtained in E-MOSAICS exhibit strong galaxy-to-galaxy variations, resulting from differences in their evolutionary histories. By correlating several metrics describing the GC age–metallicity distributions of the 25 simulated galaxies with quantities describing their formation and assembly histories (such as halo properties, formation and assembly redshifts, stellar mass assembly time-scales, numbers of major and minor mergers, redshift distribution of mergers), we identify a set of 20 correlations with high statistical significance. These correlations show that the GC age–metallicity distribution is a sensitive probe of the host galaxy's stellar mass growth, metal enrichment, and minor merger

history. Moreover, it is shown that the mass dependence of galaxy evolution in age–metallicity space enables the use of individual GCs to infer the masses and metallicities of their natal galaxies as a function of redshift. We demonstrate that this can be used to reconstruct the merger tree of the host galaxy. Applying any of these individual results to the GC population of the Milky Way may already significantly increase our understanding of its formation and assembly history. In this paper, we take the comprehensive approach of employing the full range of analysis tools presented in Kruijssen et al. (2019) to infer how the Galaxy formed and assembled.

This method represents a critical first step in our ongoing efforts to unlock the potential of GCs as quantitative tracers of galaxy formation and assembly. However, its applicability is presently restricted to a handful of galaxies due to observational limitations. Even with current state-of-the-art observatories and stellar population synthesis models, the main obstacle in applying our framework is the availability of reliable GC ages. The precision of GC age measurements is a strong function of distance due to the different methods involved, with uncertainties of $\sigma(\tau) = 1$–2 Gyr in the Milky Way ($D \sim 10$ kpc, Dotter et al. 2010; Dotter, Sarajedini & Anderson 2011; VandenBerg et al. 2013), $\sigma(\tau) \sim 2$ Gyr in the Large Magellanic Cloud (LMC; $D \sim 50$ kpc, Wagner-Kaiser et al. 2017), and $\sigma(\tau) \sim 4$ Gyr in the dwarf galaxy NGC 4449 ($D \sim 3.8$ Mpc, Annibali et al. 2018). For the foreseeable future, the Milky Way, the LMC, and possibly M31 are thus the most suitable targets for applying our technique. [2]

For galaxies with reliable GC age measurements, the potential of using the GC age–metallicity distribution for constraining galaxy formation and assembly histories is clear. In this work, we therefore apply our framework to the GC population of the Milky Way. As will be shown below, this provides important new insights into the formation and assembly history of our host galaxy.

2 COSMOLOGICAL ZOOM-IN SIMULATIONS OF GC POPULATIONS AND THEIR HOST GALAXIES

In this work, we interpret the age–metallicity distribution of Galactic GCs in terms of the Milky Way's formation and assembly history using the E-MOSAICS simulations of Milky Way-mass galaxies and their GC populations (Pfeffer et al. 2018; Kruijssen et al. 2019). These simulations combine the MOSAICS model for cluster formation and evolution (Kruijssen et al. 2011; Pfeffer et al. 2018) with the EAGLE model for galaxy formation simulations (Schaye et al. 2015; Crain et al. 2015). All simulations adopt a Lambda cold dark matter (ΛCDM) cosmogony, described by the parameters advocated by the Planck Collaboration I (2014), namely $\Omega_0 = 0.307$, $\Omega_b = 0.04825$, $\Omega_\Lambda = 0.693$, $\sigma_8 = 0.8288$, $n_s = 0.9611$, $h = 0.6777$, and $Y = 0.248$. Before proceeding, we briefly summarize the physical ingredients contained in these models.

2.1 Summary of the models

EAGLE uses a modified version of the *N*-body TreePM smoothed particle hydrodynamics code GADGET 3 (last described by Springel

---

[1]This is an acronym for 'MOdelling Star cluster population Assembly In Cosmological Simulations within EAGLE'.

[2]This adds to the growing body of literature showing that decreasing the uncertainties on GC ages from resolved or integrated-light spectroscopy is one of the most pressing open problems in GC research (also see Forbes et al. 2018 for a recent discussion).

2005) and includes a wide array of subgrid routines for modelling the baryonic physics governing galaxy formation and evolution. Most importantly, these include radiative cooling and photoionization heating (Wiersma, Schaye & Smith 2009a), a redshift-dependent UV background (Haardt & Madau 2001), stochastic star formation within gas with density above a metallicity-dependent threshold (Schaye 2004; Schaye & Dalla Vecchia 2008), stellar feedback (Dalla Vecchia & Schaye 2012), metal enrichment (Wiersma et al. 2009b), the growth of supermassive black holes by gas accretion and merging (Springel, Di Matteo & Hernquist 2005; Rosas-Guevara et al. 2015; Schaye et al. 2015), and feedback from active galactic nuclei (Booth & Schaye 2009; Schaye et al. 2015). The application of this galaxy formation model in EAGLE broadly reproduces the evolution of galaxy stellar masses and sizes (Furlong et al. 2015, 2017), their photometric properties (Trayford et al. 2015) and cold gas content (e.g. Lagos et al. 2015; Bahé et al. 2016; Crain et al. 2017), and key properties of the circumgalactic medium (e.g. Rahmati et al. 2015; Oppenheimer et al. 2016).

In E-MOSAICS, the EAGLE galaxy formation model is combined with the MOSAICS cluster model. Stellar clusters are formed as a subgrid component of newborn stellar particles based on the local gas properties at the time of their formation. The fraction of star formation occurring in bound clusters (the cluster formation efficiency, Bastian 2008; Goddard, Bastian & Kennicutt 2010) is environmentally dependent according to the model of Kruijssen (2012). The initial cluster mass function follows a power law with a universal slope of -2 between $M = 10^2 \, \mathrm{M_\odot}$ and an environmentally dependent upper mass scale from Reina-Campos & Kruijssen (2017). Both the cluster formation efficiency and the upper cluster mass scale increase with the gas pressure, implying that actively star-forming environments such as high-redshift galaxies or local-Universe galaxy mergers form a larger fraction of their mass in clusters and also form more massive ones than in low-pressure environments (see recent reviews by Kruijssen 2014; Forbes et al. 2018). This cluster formation model has been shown to reproduce a wide range of observations (e.g. Adamo et al. 2015; Johnson et al. 2016; Freeman et al. 2017; Ward & Kruijssen 2018; Messa et al. 2018).

The clusters evolve in an environmentally dependent fashion according to four disruption mechanisms. Firstly, stellar clusters can lose up to 40 per cent of their mass by stellar evolution, for which we adopt the model natively used in EAGLE. Secondly, we model the mass loss due to tidal shocks from the interstellar medium (ISM) by calculating the tidal tensor on the fly at the position of each cluster (Kruijssen et al. 2011). E-MOSAICS thus self-consistently captures the disruptive power of the different galactic environments experienced by a cluster throughout its lifetime, which provides a much improved description of tidal disruption relative to previous work. However, the absence of a cold ISM in EAGLE causes cluster disruption by tidal shocks to be underestimated in environments with low and intermediate gas pressures ($P/k < 10^7 \, \mathrm{K \, cm^{-3}}$, see Pfeffer et al. 2018). Tidal shocks are still the dominant disruption mechanism in high-pressure environments. Thirdly, we include mass loss by two-body interactions between the stars in a cluster (see also Lamers et al. 2005, Kruijssen et al. 2011). This mechanism is relevant in low-density environments, where the ISM is not as disruptive. Finally, we include a post-processing model for the destruction of the most massive clusters due to dynamical friction (Pfeffer et al. 2018). This cluster disruption model has been shown to reproduce observed cluster age distributions, mass distributions, spatial distributions, and kinematics (Kruijssen et al. 2011, 2012; Miholics, Kruijssen & Sills 2017; Adamo & Bastian 2018).

2.2 Simulated galaxy properties and suitability for comparison to the Milky Way

The E-MOSAICS suite contains 25 zoom-in simulations of all Milky Way-mass galaxies in the EAGLE Recal-L025N0752 volume, spanning present-day halo masses of $7 \times 10^{11} < M_{200}/\mathrm{M_\odot} < 3 \times 10^{12}$. This is an unbiased and volume-limited galaxy sample, with no selection on any other galaxy properties. As shown by Pfeffer et al. (2018) and Kruijssen et al. (2019), these galaxies cover a wide range of formation and assembly histories, making it the ideal reference sample for inferring the formation and assembly history of the Milky Way from the observed properties of the Galactic GC population. We demonstrate the suitability of the E-MOSAICS galaxies for this purpose in Table 1, which shows that the key physical properties of the Milky Way are consistent with those spanned by the simulated galaxies. Specifically, we show the halo mass, stellar mass, star-forming gas mass (cf. atomic and molecular gas), non-star-forming gas mass (cf. hot halo gas), current star formation rate (SFR), stellar bulge mass, bulge-to-total stellar mass ratio, stellar disc mass (cf. the combined thin and thick stellar disc), and the stellar disc scale radius. To isolate the stellar disc of each galaxy, we select all stellar particles with specific angular momentum $J_z/J_{\mathrm{circ}} > 0.5$ (cf. fig. 2 of Abadi et al. 2003).

Table 1 shows that the properties of the Milky Way are generally well reproduced by the suite of simulations. The halo mass, star-forming gas mass, non-star-forming gas mass, SFR, bulge mass bulge-to-total mass ratio, and disc scale radius all fall unambiguously within the range of values found in the E-MOSAICS galaxies. The total stellar mass and the stellar disc mass of the Milky Way slightly exceed the largest value found in the simulations, but are still consistent with the covered range to within the uncertainties of the observations. EAGLE is known to underestimate the stellar masses of Milky Way-mass dark matter haloes by up to a factor of two (see figs 4 and 8 of Schaye et al. 2015). Given that the stellar (disc) mass is the only marginally discrepant property of the simulated galaxies, we do not expect this to significantly influence the results presented in this work. None the less, it should be kept in mind when interpreting our findings.

Across the sample, good analogues of the Milky Way (here defined as matching at least six out of nine properties to within a factor of two) are MW02, MW03, MW09, MW12, MW14, and MW23. However, the variety of properties listed in Table 1 and the lack of significant correlations between them also shows that a large enough sample of simulated galaxies should eventually host a perfect Milky Way analogue. Because the observed properties of the Milky Way are consistent with the range spanned by the 25 simulated galaxies, reproducing an exact copy of the Milky Way is therefore not required for the analysis performed in this work.

3 THE OBSERVED GALACTIC GC AGE–METALLICITY DISTRIBUTION

The literature holds several compilations of the ages and metallicities of Galactic GCs (e.g. Marín-Franch et al. 2009; Dotter et al. 2010; Forbes & Bridges 2010; Dotter et al. 2011; VandenBerg et al. 2013). Here, we compile and combine three main compilations, i.e. those by Forbes & Bridges (2010),[3] Dotter et al. (2010, 2011), and VandenBerg et al. (2013). When combining these samples, we take

---

[3]The compilation by Forbes & Bridges (2010) is based on original GC age measurements by Salaris & Weiss (1998), Bellazzini, Ferraro & Ibata (2002), Catelan et al. (2002), De Angeli et al. (2005), Dotter, Sarajedini

Table 1. Properties of the 25 Milky Way-mass $L*$ galaxies at $z = 0$ in the cosmological zoom-in simulations considered in this work. From left to right, the columns show simulation ID; log halo mass; log stellar mass; log star-forming gas mass; log non-star-forming gas mass; SFR averaged over the last 300 Myr; log bulge mass; bulge-to-total mass ratio; log stellar disc mass; stellar disc scale radius; log stellar halo mass. All of the integrated baryonic galaxy properties are measured within 30 proper kpc. To give an indication of the typical values and dynamic ranges, we also include four rows listing the minimum, median, and maximum values, as well as the interquartile range of each column. For reference, the final row shows the properties of the Milky Way from Bland-Hawthorn & Gerhard (2016) including the uncertainties, where M_d includes both the thin disc and the thick disc, and R_d represents the mass-weighted average scale length of the total disc. The Milky Way's cold gas mass (M_{SF}) is taken from Nakanishi & Sofue (2016). This table shows that the Milky Way is consistent with the range of properties spanned by the E-MOSAICS galaxies.

Name	$\log M_{200}$ [$M_\odot$]	$\log M_*$ [$M_\odot$]	$\log M_{SF}$ [$M_\odot$]	$\log M_{NSF}$ [$M_\odot$]	SFR [$M_\odot$ yr^{-1}]	$\log M_b$ [$M_\odot$]	M_b/M_*	$\log M_d$ [$M_\odot$]	R_d [kpc]
MW00	11.95	10.28	9.39	10.34	0.63	9.67	0.24	10.16	6.40
MW01	12.12	10.38	9.55	11.05	0.93	10.16	0.62	9.96	3.13
MW02	12.29	10.56	9.82	11.19	1.65	9.85	0.19	10.47	7.36
MW03	12.17	10.42	9.82	11.04	1.72	9.83	0.26	10.29	6.53
MW04	12.02	10.11	9.29	10.84	0.35	9.71	0.39	9.90	5.11
MW05	12.07	10.12	8.51	10.32	0.08	9.76	0.44	9.87	2.15
MW06	11.96	10.31	9.89	10.86	2.44	9.62	0.20	10.21	4.91
MW07	11.86	10.16	9.81	10.86	1.52	9.67	0.33	9.98	3.92
MW08	11.87	10.12	9.34	10.78	1.08	9.45	0.21	10.02	2.99
MW09	11.87	10.16	9.62	10.52	1.36	9.68	0.33	9.98	4.42
MW10	12.36	10.48	9.47	11.38	0.93	10.26	0.61	10.07	3.85
MW11	12.15	10.06	9.26	11.04	0.63	9.90	0.69	9.56	2.24
MW12	12.34	10.44	9.69	11.36	1.13	10.12	0.47	10.16	4.75
MW13	12.38	10.37	8.81	11.22	0.49	9.85	0.30	10.21	2.72
MW14	12.34	10.59	9.70	11.45	1.91	10.23	0.44	10.34	3.85
MW15	12.16	10.15	9.78	10.99	2.15	10.02	0.74	9.56	3.95
MW16	12.32	10.54	7.16	10.40	0.00	10.43	0.77	9.90	2.33
MW17	12.29	10.49	9.42	10.97	0.57	10.31	0.67	10.00	2.76
MW18	12.25	10.00	9.40	10.75	1.31	9.80	0.63	9.57	6.09
MW19	12.20	9.93	9.64	11.20	1.13	9.64	0.52	9.61	6.90
MW20	11.97	10.10	9.60	11.04	0.71	9.69	0.38	9.89	3.87
MW21	12.12	10.03	9.25	10.60	0.50	9.94	0.82	9.30	6.20
MW22	12.15	10.43	7.55	10.33	0.00	10.33	0.80	9.73	3.39
MW23	12.19	10.53	9.97	11.24	3.30	9.94	0.26	10.40	6.55
MW24	12.06	10.29	9.40	10.74	0.65	9.93	0.43	10.05	2.62
Minimum	11.86	9.93	7.16	10.32	0.00	9.45	0.19	9.30	2.15
Median	12.15	10.29	9.47	10.97	0.93	9.85	0.44	9.98	3.92
Maximum	12.38	10.59	9.97	11.45	3.30	10.43	0.82	10.47	7.36
IQR	0.27	0.32	0.41	0.45	0.95	0.43	0.33	0.29	3.10
Milky Way	12.04 ± 0.12	10.7 ± 0.1	9.9 ± 0.1	10.40 ± 0.18	1.65 ± 0.19	10.19 ± 0.04	0.30 ± 0.06	10.54 ± 0.16	2.5 ± 0.4

the mean ages and metallicities whenever multiple measurements are available, resulting in a total of 96 GCs. A table listing these quantities and their uncertainties for the full sample of GCs is provided in Appendix A. Before proceeding, we remove all GCs with masses $M < 10^5\,M_\odot$ and [Fe/H] > -0.5 to match the selection criteria used when analysing the E-MOSAICS simulations in Kruijssen et al. (2019), leaving 61 GCs. This mass selection is made to minimize the effects of GC disruption, which is underestimated in E-MOSAICS at lower GC masses in particular (see Pfeffer et al. 2018), whereas the metallicity range is chosen to maximize the completeness of the available GC age measurements. For reference, the total number of Galactic GCs with $M \geq 10^5\,M_\odot$ (assuming $M_{V,\odot} = 4.83$ and $M/L_V = 2$) and $-2.5 <$ [Fe/H] < -0.5 is $N_{GC} = 78$ (Harris 1996, 2010 edition), showing that our sample contains 78 per cent of the available GCs and is thus relatively complete. This completeness does not depend strongly on metallicity, as the sample includes $\sim$70 per cent of the available GCs at [Fe/H] ≤ -1.5 and $\sim$90 per cent at $-1.5 <$ [Fe/H] < -0.5.

Fig. 1 shows the distributions of GCs from the four samples in age–metallicity space, including a set of quantitative metrics for describing the GC age–metallicity distribution derived in Kruijssen et al. (2019, section 3.2; also see below). The age uncertainties are based on the original GC compilations. In addition, we adopt a fiducial metallicity uncertainty of σ([Fe/H]) $= 0.1$ dex. Qualita-

tively, the GC age–metallicity distributions have a similar structure, with a steep branch at old ages, covering all metallicities, and a well-populated branch at intermediate metallicities that extends to young ages. The former branch includes mostly GCs at small galactocentric radii that are associated with the Galactic bulge, whereas the latter branch hosts mainly halo GCs, some of which are associated with tidal debris from satellite accretion. Indeed, in Kruijssen et al. (2019) we show that the old branch mostly traces the *in situ* growth of the main progenitor galaxy, whereas the young branch is constituted by GCs that formed *ex situ*. Therefore, we refer to these branches as the 'main branch' and the 'satellite branch', respectively. Fig. 1 thus illustrates that the Milky Way acquired a significant part of its GC population through satellite accretion (see e.g. Leaman et al. 2013).

There exist some quantitative differences between the four samples shown in Fig. 1, most notably in their completeness and absolute age calibration, but there is no evidence for any strong systematic uncertainties. The bottom-right panel of Fig. 1 shows the combined mean catalogue and contains markedly less scatter around the satellite branch than each of the three individual samples. This suggests that the uncertainties are predominantly statistical rather than systematic, unless systematic errors affect all age measurements in the same way, and motivates using the combined mean sample when inferring the formation and assembly history of the Milky Way. We will therefore restrict our analysis to the 'combined mean' GC sample throughout this paper.

Following section 3.2 of Kruijssen et al. (2019), we list 13 quantitative metrics describing the GC age–metallicity distributions

& Yang (2008), Carraro, Zinn & Moni Bidin (2007), Carraro (2009), and Marín-Franch et al. (2009).
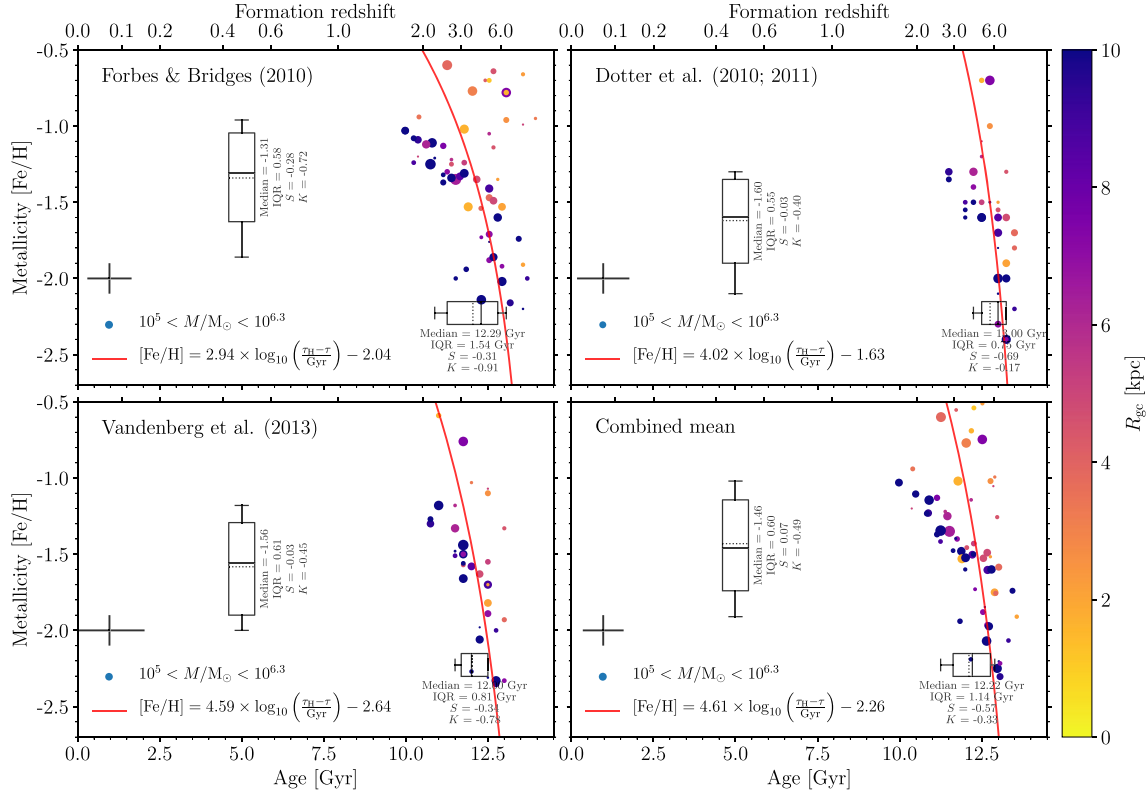
Figure 1. Observed age–metallicity distributions of GCs in the Milky Way according to the compilations of Forbes & Bridges (2010, top left panel), Dotter et al. (2010, 2011, top right panel), VandenBerg et al. (2013, bottom left panel) and the combined mean of all three samples (bottom right panel). The symbol colour indicates the galactocentric radius according to the colour bar and the symbol size reflects the logarithm of the GC mass across the mass range indicated in each panel. Each age–metallicity distribution is characterized through two box plots and interquartile ranges of both age and metallicity, as well as by fitting the function shown in the bottom left corner of each panel (red line), with the best-fitting forms indicated (where $\tau_H = 13.82$ Gyr represents the age of the Universe). The various compilations are qualitatively similar, such that they can be used to constrain the formation and assembly history of the Milky Way.

in Table 2. Several of these are also shown visually in Fig. 1. The number of GCs N'_{GC} refers to all Galactic GCs with present-day masses of $M > 10^5 M_\odot$ (using $M_{V,\odot} = 4.83$ and $M/L_V = 2 M_\odot L_\odot^{-1}$) and metallicities $-2.5 < [Fe/H] < -0.5$ listed in the Harris (1996, 2010 edition) catalogue, irrespective of whether they are included in any of the listed literature samples. As listed, most of these metrics do not account for the uncertainties on the GC ages and metallicities. The only two exceptions are the age–metallicity slope $d[Fe/H]/d \log t$ and intercept $[Fe/H]_0$, which have been obtained using an orthogonal distance regression (Boggs & Rogers 1990) of the data with error bars. For the relevant subset of quantities, we obtain uncertainties in Section 4.1 below. The numbers listed in Table 2 confirm the visual impression from Fig. 1 that the GC age–metallicity distributions are qualitatively similar across all samples.

We can compare the metrics listed in Table 2 describing the GC age–metallicity distribution of the Milky Way to those of the 25 simulated galaxies in the E-MOSAICS suite listed in table 2 of Kruijssen et al. (2019), of which the statistics are listed in the final four rows of Table 2. The Milky Way GCs are old, with a somewhat narrow age distribution that has a normal skewness, but has underrepresented wings relative to its standard deviation (i.e. a negative kurtosis), indicating an extended episode of GC formation over their full age range. The GC metallicities are lower than the median across the simulations,[4] with considerably less absolute

skewness than most of the simulated galaxies, but an otherwise ordinary metallicity distribution around the median. As a result, the Milky Way GC population is also relatively 'average' in terms of the combined interquartile range IQR^2 and the IQR aspect ratio r_{IQR}. The best fits to the GC age–metallicity distribution are a bit steeper than average and attain a higher metallicity after 1 Gyr than most of the simulations do, indicating a relatively early collapse of the Galactic dark matter halo and rapid metal enrichment. Finally, the number of GCs is also slightly higher than average, with a median $N'_{GC} = N_{GC}/f_{corr} = 59$ for the simulations (where $f_{corr} = 1.75$ is a correction factor to account for the fact that GC disruption is underestimated in E-MOSAICS; see the discussion in Kruijssen et al. 2019).[5] Despite these small differences relative to the median

This manifests itself most strongly at low gas pressures, which are found predominantly in the low-redshift discs where metal-rich clusters are formed. As a result, E-MOSAICS overpredicts the number of metal-rich GCs. However, this mostly occurs outside the metallicity range that is spanned by the observations and is considered here. The metallicity offset between the observations and simulations may also reflect a difference in calibration, or be caused by uncertainties on the nucleosynthetic yields in the simulations. Together, these introduce a systematic uncertainty of a factor of 2 (Schaye et al. 2015). Perhaps most importantly, the (absolute) median metallicity is not found to correlate with any galaxy-related quantities in Kruijssen et al. (2019), which means that it will not be used in the remainder of this work.

---

[4]This is possibly a result of the fact that GC disruption is underestimated in E-MOSAICS due to the limited resolution (see Pfeffer et al. 2018).

[5]In part, the somewhat lower number of GCs in the E-MOSAICS galaxies relative to the Milky Way may be caused by the fact that EAGLE

Table 2. Quantities describing the GC age–metallicity distributions in the four (sub)samples of Galactic GCs. From left to right, the columns list the following: GC sample; median GC age $\widetilde{\tau}$ in Gyr; GC age interquartile range $\mathrm{IQR}(\tau)$ in Gyr; GC age skewness $S(\tau)$; GC age excess kurtosis $K(\tau)$; median GC metallicity $\widetilde{[\mathrm{Fe/H}]}$; GC metallicity interquartile range $\mathrm{IQR}([\mathrm{Fe/H}])$; GC metallicity skewness $S([\mathrm{Fe/H}])$; GC metallicity excess kurtosis $K([\mathrm{Fe/H}])$; combined interquartile range $\mathrm{IQR}^2 \equiv \mathrm{IQR}(\tau) \times \mathrm{IQR}([\mathrm{Fe/H}])$ in Gyr; interquartile range aspect ratio $r_{\mathrm{IQR}} \equiv \mathrm{IQR}([\mathrm{Fe/H}])/\mathrm{IQR}(\tau)$ in Gyr^{-1}; best-fitting slope $\mathrm{d[Fe/H]/d\log}t$ of the function fitted in Fig. 1 indicating the rapidity of metal enrichment in the progenitor galaxies as traced by GCs; best-fitting intercept $[\mathrm{Fe/H}]_0$ of the function fitted in Fig. 1 indicating the typical 'initial' GC metallicity at 1 Gyr after the Big Bang; number of GCs (defined as clusters with present-day masses of $M > 10^5\,\mathrm{M}_\odot$) in the metallicity range $-2.5 < [\mathrm{Fe/H}] < -0.5$ (Harris 1996, 2010 edition) that is considered throughout this work. The first four rows consider the observed GC samples from Fig.1, i.e. from Forbes & Bridges (2010, FB10), Dotter et al. (2010, 2011, D11), VandenBerg et al. (2013, V13), and the combined sample (see Appendix A). To give an indication of the typical variation between these GC samples and the 25 simulated galaxies from E-MOSAICS, the final rows list the minimum, median, maximum, and interquartile range of each column, both for the observed Galactic GC age–metallicity distribution and the modelled GC age–metallicity distributions in E-MOSAICS.

Name	$\widetilde{\tau}$	$\mathrm{IQR}(\tau)$	$S(\tau)$	$K(\tau)$	$\widetilde{[\mathrm{Fe/H}]}$	$\mathrm{IQR}([\mathrm{Fe/H}])$	$S([\mathrm{Fe/H}])$	$K([\mathrm{Fe/H}])$	IQR^2	r_{IQR}	$\frac{\mathrm{d[Fe/H]}}{\mathrm{d}\log t}$	$[\mathrm{Fe/H}]_0$	N'_{GC}
					Observed Galactic GC age–metallicity distribution								
FB10	12.30	1.54	−0.31	−0.91	−1.31	0.58	−0.28	−0.72	0.90	0.38	2.94	−2.04	78
D11	13.00	0.75	−0.69	−0.17	−1.60	0.55	−0.03	−0.40	0.41	0.73	4.02	−1.63	78
V13	12.00	0.81	−0.34	−0.78	−1.56	0.61	−0.03	−0.45	0.49	0.75	4.59	−2.64	78
Combined	12.22	1.14	−0.57	−0.33	−1.46	0.60	0.07	−0.49	0.68	0.52	4.61	−2.26	78
Minimum	12.00	0.75	−0.69	−0.91	−1.60	0.55	−0.28	−0.72	0.41	0.38	2.94	−2.64	78
Median	12.26	0.97	−0.46	−0.55	−1.51	0.59	−0.03	−0.47	0.59	0.63	4.31	−2.15	78
Maximum	13.00	1.54	−0.31	−0.17	−1.31	0.61	0.07	−0.40	0.90	0.75	4.61	−1.63	78
IQR	0.31	0.44	0.27	0.52	0.15	0.03	0.09	0.12	0.26	0.25	0.85	0.42	0
					Modelled GC age–metallicity distributions in E-MOSAICS								
Minimum	7.90	0.44	−3.15	−1.16	−1.59	0.33	−1.67	−1.07	0.22	0.20	2.33	−3.90	29
Median	10.73	1.39	−0.51	0.63	−0.91	0.69	−0.93	−0.11	1.06	0.55	3.50	−2.69	59
Maximum	12.45	3.46	0.71	28.09	−0.71	0.88	0.18	2.18	2.42	1.11	6.58	−1.69	187
IQR	1.01	1.12	1.79	4.15	0.12	0.22	0.44	0.99	0.73	0.27	1.32	0.53	72

properties of the simulated GC populations, we find that the ranges spanned by the simulations contain the Milky Way values without exception. This shows that the framework developed in Kruijssen et al. (2019) for inferring the formation and assembly histories of galaxies from their GC populations can be applied to the Milky Way.

4 RECONSTRUCTING THE FORMATION AND ASSEMBLY OF THE GALAXY

4.1 Statistical description of the inferred formation and assembly history of the Milky Way

In Kruijssen et al. (2019), we systematically explore the correlations between the 13 quantities describing the GC age–metallicity distribution and a set of 30 quantities describing the formation and assembly of the host galaxy, for the entire sample of 25 Milky Way-mass galaxies in E-MOSAICS. Out of the 390 correlations evaluated, 20 are found to carry a high statistical significance.[6] The best-fitting linear and power-law relations are listed in table 7 of Kruijssen et al. (2019) and can be used to derive the galaxy-related quantities from the observed properties of the Galactic GC population. The 20 significant correlations rely on five GC-related quantities, i.e. the

underestimates the stellar masses of Milky Way-mass haloes by up to a factor of two (see the discussion in Section 2). Depending on when this additional stellar mass would have formed, it could plausibly have contributed a number of GCs. Accounting for this missing mass in the simulations could thus increase the number of GCs, at most by a factor of two.

[6]Additional correlations exist, but here we restrict our analysis to the strongest ones, because these are unambiguously physical in nature rather than a statistical coincidence. We emphasize that the relations adopted here are not the result of underlying dependences on the halo mass (M_{200}) or other quantities against which possible correlations of the GC age–metallicity distribution are tested in Kruijssen et al. (2019). Specifically for M_{200}, we find no statistically significant correlations due to the narrow range in halo mass covered by the E-MOSAICS simulations. See Kruijssen et al. (2019) for further details.

median GC age $\widetilde{\tau}$, the GC age interquartile range $\mathrm{IQR}(\tau)$, the interquartile range aspect ratio $r_{\mathrm{IQR}} \equiv \mathrm{IQR}([\mathrm{Fe/H}])/\mathrm{IQR}(\tau)$, the best-fitting slope of the GC age–metallicity distribution $\mathrm{d[Fe/H]/d\log}t$, and the number of GCs N'_{GC} (as before, these are restricted to masses $M > 10^5\,\mathrm{M}_\odot$ and metallicities $-2.5 < [\mathrm{Fe/H}] < -0.5$). Together, these metrics trace a total of 12 galaxy-related quantities. This is less than the 20 correlations, because some quantities are inferred through more than one GC-related metric.

The first set of six galaxy-related quantities describes the instantaneous properties and the mass growth history of the galaxy, i.e. the maximum circular velocity V_{max}, the concentration parameter of the dark matter halo profile c_{NFW}, the lookback times at which the main progenitor attains $\{25, 50\}$ per cent of its maximum halo mass $\{\tau_{25}, \tau_{50}\}$, the redshift at which the *main progenitor* reaches 50 per cent of its final stellar mass z_a, and the lookback time at which 50 per cent of all stars currently in the galaxy have formed *across all progenitors* τ_f.[7] The second set describes the merger history and progenitor population of the galaxy, i.e. the number of high-redshift ($z > 2$) mergers experienced by the main progenitor $N_{\mathrm{br},z>2}$, its total number of mergers N_{br}, the fraction of $z > 2$ mergers $r_{z>2}$, the total number of progenitors N_{leaf}, the number of 'tiny' mergers (with stellar mass ratio $<1{:}100$) $N_{<1:100}$, and the number of minor mergers (with stellar mass ratio $1{:}4$–$1{:}100$) $N_{1:4-1:100}$. In this framework, 'major' mergers are considered those with stellar mass ratios $>1{:}4$. Note that these quantities only include progenitors with stellar masses $M_* > 4.5 \times 10^6\,\mathrm{M}_\odot$, to restrict the statistics of the progenitors to haloes hosting at least 20 stellar particles.

[7]These lookback times are chosen as 'distance markers' along the Milky Way's continuous formation and assembly history, and deliberately deviate from the classical narrative of 'two-phase' galaxy formation, which oversimplifies the complexity of galaxy assembly through a sharp separation between *in situ* and *ex situ* growth. Especially at the peak formation redshifts of GCs ($z = 2$–6, Forbes et al. 2015; Reina-Campos et al. 2018a), this distinction is highly ambiguous, because the intense merging activity at these redshifts can be an important driver of *in situ* star formation by bringing gas into the main progenitor.
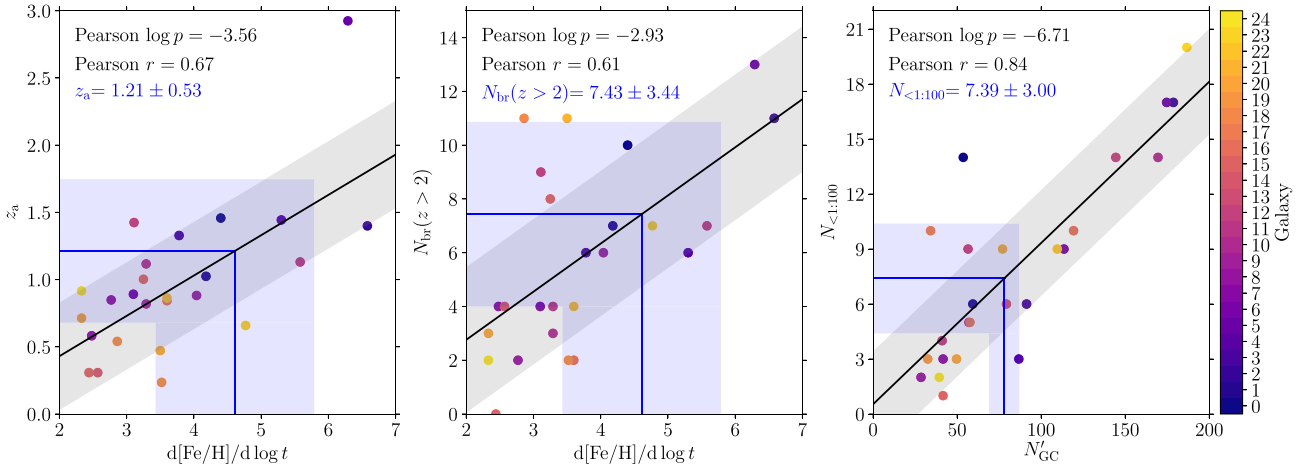
Figure 2. Examples of three statistically significant correlations between galaxy formation and assembly-related quantities from Kruijssen et al. (2019, section 4.2) (*y*-axes) and the quantities describing the GC age–metallicity distribution from Kruijssen et al. (2019, section 3.2) (*x*-axes). Left panel: galaxy assembly redshift z_a, which indicates when the main progenitor first attains 50 per cent of the galaxy's stellar mass at $z = 0$, as a function of the best-fitting slope of the GC age–metallicity distribution $d[Fe/H]/d\log t$. Middle panel: number of high-redshift ($z > 2$) mergers $N_{br,z>2}$ as a function of $d[Fe/H]/d\log t$. Right panel: number of tiny mergers $N_{<1:100}$ (note that galaxies with stellar masses $M < 4.5 \times 10^6\,M_\odot$ are not counted as discrete mergers, but as smooth accretion), as a function of the (corrected) number of GCs N'_{GC} (see the text) in the mass and metallicity range $M > 10^5\,M_\odot$ and $-2.5 < [Fe/H] < -0.5$. Coloured symbols denote the 25 simulations as indicated by the colour bar on the right. In each panel, the solid line indicates the best-fitting linear regression, with the grey-shaded band marking the 1σ scatter of the data around the fit, and the Pearson *p*-values and correlation coefficients in the top-left corner indicating its statistical significance. The blue bands show how the quantities are inferred from the age–metallicity distribution of Galactic GCs in the bottom-right panel of Fig. 1. Together, these place quantitative constraints on the formation and assembly history of the Milky Way.

In order to determine the uncertainties of the obtained galaxy-related quantities, we must estimate the uncertainties on the five GC-related quantities that they are derived from. For $\tilde{\tau}$, $IQR(\tau)$, and r_{IQR}, we obtain these by Monte Carlo sampling 10^5 different realizations of the 'combined mean' Galactic GC age–metallicity distribution (bottom-right panel of Fig.1), using the age and metallicity uncertainties of each individual GC and measuring the quantities for each realization. The resulting distributions are close to Gaussian and we therefore adopt the standard deviations across the 10^5 realizations as the uncertainties. For the age interquartile range $IQR(\tau)$, which measures the age dispersion of the GC sample, we subtract the mean age error of the GCs in quadrature to avoid artificially boosting the underlying interquartile range. The resulting median metrics and their uncertainties are $\{\tilde{\tau}, IQR(\tau), r_{IQR}\} = \{12.21 \pm 0.12, 1.21 \pm 0.20, 0.48 \pm 0.10\}$. These values are very similar to the numbers listed for the combined mean sample in Table 2, which were derived without accounting for the uncertainties on the data. For the slope of the GC age–metallicity distribution $d[Fe/H]/d\log t$, the uncertainties are obtained self-consistently from the weighted orthogonal distance regression to the data with their age–metallicity uncertainties, resulting in $d[Fe/H]/d\log t = 4.61 \pm 1.18$ (or $\log d[Fe/H]/d\log t = 0.664 \pm 0.112$). Finally, for the number of GCs, we assume Poisson errors, i.e. $N'_{GC} = 78 \pm 9$ (or $\log N'_{GC} = 1.892 \pm 0.049$).

We now combine the above metrics describing the GC age–metallicity distributions with the best-fitting relations from table 7 of Kruijssen et al. (2019) connecting them to several galaxy-formation-related quantities to constrain the formation and assembly history of the Milky Way. Fig. 2 shows three examples, highlighting the relations between the slope of the GC age–metallicity distribution ($d[Fe/H]/d\log t$) and the assembly redshift (z_a, left) and number of high-redshift mergers ($N_{br,z>2}$, middle), as well as between the number of GCs (N'_{GC}) and the number of tiny mergers ($N_{<1:100}$, right). These relations show that the uncertainties are sufficiently

small to provide meaningful constraints on the formation history of the Milky Way. Fig. 2 confirms the picture sketched in Section 3, in which the Milky Way assembled early – with $z_a = 1.2 \pm 0.5$, its fiducial assembly redshift (at which 50 per cent of the $z = 0$ stellar mass is first attained by the main progenitor) corresponds to the 76th percentile of the 25 simulations shown as coloured symbols.[8] The number of high-redshift mergers $N_{br,z>2}$ is also larger than the median across the E-MOSAICS suite (72th percentile), again indicative of an early formation and assembly phase. By contrast, the total number of tiny mergers implied by N'_{GC} is $N_{<1:100} = 7.4 \pm 3.0$, which is close to the median of our sample of simulated galaxies. It is thus not the number of accretion events experienced by the Milky Way that is elevated, but the lookback time at which these mergers took place that is larger than for most other galaxies.

Table 3 lists the complete set of metrics describing the formation and assembly history of the Milky Way that we obtain using the Galactic GC population. Reassuringly, the quantities for which we have multiple independent constraints all match to within the uncertainties. Physically, the combination of all quantities paints a consistent picture. Within our sample, the Milky Way has a typical mass and rotation curve, as indicated by the fact that the maximum circular velocity $V_{max} = 180 \pm 17\,km\,s^{-1}$ implied by the number of GCs[9] and the concentration parameter $c_{NFW} = 8.0 \pm 1.0$ obtained from $IQR(\tau)$, r_{IQR}, and N'_{GC} both correspond to the 48th percentiles of our simulations.

---

[8]The outlier at $z_a \sim 3$ is galaxy MW05, which quenches at $z \sim 2$ and as a result has an assembly redshift biased to early cosmic times.

[9]This maximum circular velocity is inconsistent with the measured V_{max} of the Milky Way, but it matches the circular velocity at radii $R > 40$ kpc in the Galactic halo (e.g. Sofue 2015). These radii are where V_{max} is typically found in the E-MOSAICS galaxies. We interpret this as a sign of the known underestimation of the stellar masses of Milky Way-mass haloes in *EAGLE* (see the discussion in Section 2).

Table 3. Results of applying the 20 statistically significant correlations between quantities characterizing galaxy formation and assembly and those describing the GC age–metallicity distribution to the GC population of the Milky Way. For each correlation, the table lists the predicted galaxy-related value based on the properties of the Galactic GC population, including the 1σ uncertainties. For those quantities that are constrained by multiple relations, the final column shows the weighted mean. (See the text for details.)

Quantity	[Units]	Obtained from	Value	Combined
$V_{\rm max}$	[km s^{-1}]	$\log N'_{\rm GC}$	180 ± 17	
$c_{\rm NFW}$	[–]	IQR(τ)	8.5 ± 1.6	8.0 ± 1.0
$c_{\rm NFW}$	[–]	$r_{\rm IQR}$	7.6 ± 1.7	
$c_{\rm NFW}$	[–]	$\log N'_{\rm GC}$	7.9 ± 1.8	
τ_{25}	[Gyr]	$\widetilde{\tau}$	11.8 ± 1.2	11.5 ± 0.8
τ_{25}	[Gyr]	$\log {\rm d}[{\rm Fe/H}]/{\rm d}\log t$	11.2 ± 1.0	
τ_{50}	[Gyr]	$\log {\rm d}[{\rm Fe/H}]/{\rm d}\log t$	9.4 ± 1.4	
$z_{\rm a}$	[–]	${\rm d}[{\rm Fe/H}]/{\rm d}\log t$	1.2 ± 0.5	
$\tau_{\rm f}$	[Gyr]	$\widetilde{\tau}$	10.1 ± 1.4	
$N_{{\rm br},z>2}$	[–]	$\widetilde{\tau}$	9.9 ± 2.3	9.2 ± 1.9
$N_{{\rm br},z>2}$	[–]	${\rm d}[{\rm Fe/H}]/{\rm d}\log t$	7.4 ± 3.4	
$N_{\rm br}$	[–]	$r_{\rm IQR}$	14.1 ± 6.1	15.1 ± 3.3
$N_{\rm br}$	[–]	${\rm d}[{\rm Fe/H}]/{\rm d}\log t$	18.9 ± 7.4	
$N_{\rm br}$	[–]	$N'_{\rm GC}$	14.2 ± 4.7	
$r_{z>2}$	[–]	$\widetilde{\tau}$	0.61 ± 0.10	
$N_{\rm leaf}$	[–]	$\log N'_{\rm GC}$	24.1 ± 10.2	
$N_{<1:100}$	[–]	$r_{\rm IQR}$	7.1 ± 4.3	7.9 ± 2.2
$N_{<1:100}$	[–]	${\rm d}[{\rm Fe/H}]/{\rm d}\log t$	10.7 ± 5.3	
$N_{<1:100}$	[–]	$N'_{\rm GC}$	7.4 ± 3.0	
$N_{1:100-1:4}$	[–]	$\log N'_{\rm GC}$	4.4 ± 2.3	

The above picture changes when considering quantities that measure the growth rate of the Galaxy. The lookback times at which 25 and 50 per cent of the Milky Way's final halo mass are predicted to have assembled, $\tau_{25} = 11.5 \pm 0.8$ Gyr (i.e. $z = 3$) and $\tau_{50} = 9.4 \pm 1.4$ Gyr (i.e. $z = 1.5$), correspond to the 76th and 72th percentiles of the E-MOSAICS suite, respectively. For comparison, the application of the extended Press–Schechter formalism to the Planck cosmology adopted in this work shows that haloes of mass $M_{200} = 10^{12}$ M$_\odot$ reach $\{25, 50\}$ per cent of their present-day mass at redshift $z = \{2.3, 1.2\}$ (Correa et al. 2015). As with the above comparison to the E-MOSAICS galaxies, this suggests that the Milky Way assembled faster than most galaxies of its halo mass. We have already seen in Fig. 2 that the same applies to the assembly redshift, which indicates when 50 per cent of the final *stellar* mass has assembled into the main progenitor, and Table 3 extends this to the formation lookback time $\tau_{\rm f} = 10.1 \pm 1.4$ Gyr, which indicates the time at which 50 per cent of the stellar mass at $z = 0$ has been attained across all progenitors and corresponds to the 94th percentile of the sample of simulated galaxies. Comparing this to the equivalent number based on the star formation history from Snaith et al. (2014), which is $\tau_{\rm f} = 10.5 \pm 1.5$ Gyr, we see that our estimate is in excellent agreement with the more direct, star-formation-history-based measurement.

The remainder of Table 3 lists a variety of quantities describing the merger history of the Milky Way. Firstly, we predict that the Milky Way experienced $N_{{\rm br},z>2} = 9.2 \pm 1.9$ mergers before $z = 2$. Even though the total number of mergers $N_{\rm br} = 15.1 \pm 3.3$ experienced by the Milky Way is not unusually high (52nd percentile in E-MOSAICS), the number of high-redshift mergers corresponds to the 80th percentile of the simulated galaxies. This directly implies a high fraction of mergers having taken place at $z > 2$,

coincident with the ages spanned by the Galactic GC population. Indeed, $r_{z>2} = 0.61 \pm 0.10$ (88th percentile) suggests an early phase of rapid merging during which a large fraction of the Milky Way assembled. As shown in Kruijssen et al. (2019), the GC age–metallicity distribution does not strongly constrain the host galaxy's major merger activity (with stellar mass ratios $>1:4$), because the GC population is mainly shaped by minor mergers. For that reason, the final three quantities listed in Table 3 describe the minor merger history of the Milky Way. Before discussing these, we reiterate that any accreted satellites with stellar masses $M_* < 4.5 \times 10^6$ M$_\odot$ are not counted as mergers, but as smooth accretion. The total number of progenitors $N_{\rm leaf} = 24.1 \pm 10.2$ (a fraction $1 - N_{\rm br}/N_{\rm leaf} \approx 0.37$ of which merged prior to accretion onto the Milky Way) is not well constrained due to the large uncertainties, but does correspond to a rather 'normal' 48th percentile in E-MOSAICS. Likewise, the number of tiny mergers ($N_{<1:100} = 7.9 \pm 2.2$) and minor mergers ($N_{1:100-1:4} = 4.4 \pm 2.3$) are common numbers across the simulation suite, corresponding to the 52th and 40th percentiles, respectively. Subtracting the number of tiny and minor mergers from the total number of mergers leaves space for a couple (3 ± 3) of major mergers experienced by the Milky Way, which based on these numbers (e.g. $\tau_{25} = 11.5 \pm 0.8$ Gyr) most likely took place during its early, rapid-formation phase, i.e. at $\tau > 11$ Gyr or $z > 2.5$.

4.2 The inferred merger tree of the Milky Way

In Kruijssen et al. (2019), we use the E-MOSAICS simulations to develop a framework for reconstructing a galaxy's merger tree based on the age–metallicity distribution of its GC population. This approach links the ages and metallicities of the GCs to the evolution of galaxies in the phase space spanned by stellar mass, lookback time, and the metallicity of newly formed stars, for all galaxies in the EAGLE Recal-L025N0752 volume. Here, we apply this method to the GC population of the Milky Way. Fig. 3 shows the GC age–metallicity distribution of the Milky Way, with the background colour indicating the expected host galaxy stellar mass of each GC (top panel) or the number of surviving GCs expected to be brought in by a galaxy forming stars at a given age–metallicity coordinate (bottom panel). The latter is estimated based on the galaxies' projected $z = 0$ halo masses, the observed relation between the GC system mass and the dark matter halo mass at $z = 0$ ($M_{\rm GCs}/M_{200} = 3 \times 10^{-5}$, Durrell et al. 2014; Harris, Blakeslee & Harris 2017), and the mean GC mass at $M > 10^5$ M$_\odot$, which is $\overline{M} = 4.7 \times 10^5$ M$_\odot$ for a typical GC mass function (e.g. Jordán et al. 2007). This results in $N'_{\rm GC} = 10^{-10.2} \times [M_{200}(z=0)/{\rm M}_\odot]$. For reference, the vector field indicates the typical evolution of galaxies in age–metallicity space. By connecting the Galactic GCs along such flow lines to the background colour, we can infer the properties of the Milky Way's progenitors and reconstruct part of its merger tree. The top panel clearly demonstrates that GC metallicity is the strongest indicator of the mass of its host galaxy at formation, with a secondary dependence on GC age.

The main branch of the Galactic GC population shown in Fig. 3 is very steep, straddling the edge of the age–metallicity range occupied by the simulated galaxies in the EAGLE Recal-L025N0752 volume. This suggests rapid stellar mass growth and metal enrichment, which is consistent with the findings from Section 4.1. As discussed in Kruijssen et al. (2019), the stellar mass growth and metal enrichment histories of the main progenitor can be read off Fig. 3 by following the upper envelope of the GC population's
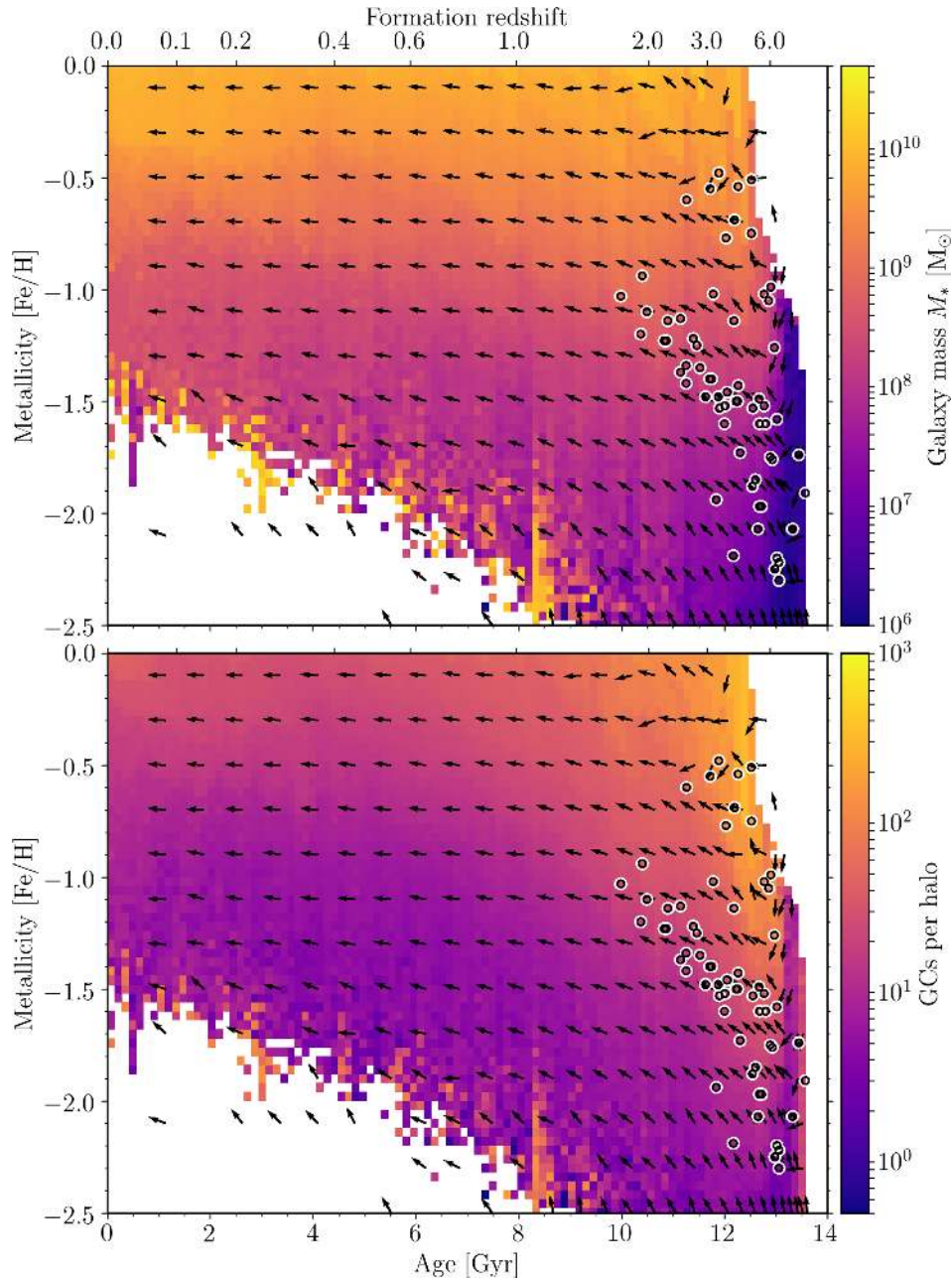
Figure 3. Age–metallicity evolution of star formation within the EAGLE Recal-L025N0752 simulation for all galaxies with halo masses $M_{200} \leq 3 \times 10^{12}\,\mathrm{M}_\odot$. Top panels: At each age–metallicity coordinate, the colour indicates the median of the host galaxy stellar mass of all star particles formed since the previous snapshot. Bottom panels: The colour indicates the median number of surviving GCs expected to be hosted at $z = 0$ by a galaxy forming stars at that age–metallicity coordinate (see the text). In both panels, vectors indicate the host's median metallicity evolution towards the next snapshot. The circles indicate the GC population of the Milky Way. In the text, we use the background colours in this figure to reconstruct the stellar mass growth history, metal enrichment history, and merger tree of the Milky Way.

main branch and subtracting $\Delta[\mathrm{Fe/H}] = 0.3$ dex.[10] Given the age range of the GC population of the main branch, this is possible for redshifts $z = 3$–6. The result is listed in Table 4, together with the expected number of GCs with mass $M > 10^5\,\mathrm{M}_\odot$ hosted by the

Galaxy at $z = 0$ as obtained from the bottom panel in Fig. 3.[11] In addition to these numbers, the correlation analysis from Section 4.1 and Table 3 revealed that 50 per cent of the Milky Way's stellar

---

[10]This downward metallicity correction is recommended in Kruijssen et al. (2019) to account for the fact that GCs have slightly higher metallicities than their host due to being born in the central regions of their host galaxy.

[11]The expected number of GCs has asymmetric uncertainties. At a given age–metallicity coordinate, the EAGLE Recal-L025N0752 volume contains a non-negligible number of host galaxies that end up with halo masses at $z = 0$ that are considerably lower than the median, which would therefore hold proportionally fewer GCs. These downwards uncertainties are typically a factor of 2 and the number of GCs in Fig. 3 should be read with this caveat

Table 4. Stellar mass growth and metal enrichment histories of the four identified (and likely most massive) Milky Way progenitors, identified using the age–metallicity distribution of Galactic GCs. We also list the number of GCs with masses $M > 10^5\,M_\odot$ expected to be hosted by each progenitor were it to survive as an undisrupted galaxy until $z = 0$. The uncertainties on the inferred stellar masses and metallicities are 0.26 and 0.25 dex, respectively (Kruijssen et al. 2019, section 5.3), unless stated otherwise.

Progenitor	z	τ/Gyr	$\log M_*/M_\odot$	[Fe/H]	N'_{GC}
Main	6	12.9	8.2	−1.3	150^{+12}_{-75}
	4	12.3	9.1	−0.8	
	3	11.7	9.5	−0.5	
	1.2 ± 0.5	$8.7^{+1.3}_{-2.2}$	$10.4^{+0.1}_{-0.1}$	0.1	
Sat 1 & 2	6	12.9	6.9	−1.8	22^{+5}_{-11}
	4	12.3	8.0	−1.6	
	3	11.7	8.2	−1.4	
	2.3	11.0	8.6	−1.2	
	1.7	10.0	9.1	−1.0	
Sat 3	6	12.9	6.3	−2.4	8^{+3}_{-4}
	4	12.3	7.0	−2.2	
	3	11.7	7.6	−1.9	

mass at $z = 0$ (which is $M_* = 5 \pm 1 \times 10^{10}\,M_\odot$; see e.g. Bland-Hawthorn & Gerhard 2016) should have assembled into the main progenitor by $z = 1.2 \pm 0.5$. We find that EAGLE galaxies reaching $M_* = 2.5 \times 10^{10}\,M_\odot$ at that redshift have typical star-forming gas metallicities of [Fe/H] = 0.1. This combination of age, mass, and metallicity thus provides an additional data point in the formation and assembly history of the Milky Way, even if our sample does not contain any GCs with such young ages.

Similar constraints can be placed on the stellar mass evolution and metal enrichment of the accreted satellites, using the GC satellite branch in Fig. 3. In Kruijssen et al. (2019) we claimed that, as a general guideline based on our 25 cosmological zoom-in simulations in E-MOSAICS, the properties of the accreted satellites can be inferred for $z = 1$–2.5 (or $\tau = 7.9$–11.2 Gyr). However, owing to the rapid growth of the Milky Way's main progenitor, the GC satellite branch separates from the main branch already at a considerably higher redshift ($z \sim 5$), enabling the satellite population to be followed over an unusually broad redshift range of $z = 1.7$–6 (or $\tau = 10$–12.9 Gyr) thanks to the vector fields shown in Fig. 3. The Milky Way's satellite branch is quite wide at $z = 3$–4 (or $\tau \sim 12$ Gyr), spanning Δ[Fe/H] = 0.9 dex from [Fe/H] = −2.2 to [Fe/H] = −1.3. This implies the existence of multiple accreted satellites of various masses. About 35 GCs are associated with a single satellite branch that extends to $z = 1.7$ and relatively high metallicities of [Fe/H] = −1.0.[12] Using the bottom panel of Fig. 3, we find that galaxies forming stars at these ages and metallicities are expected to host 22^{+5}_{-11} GCs by $z = 0$. Because star formation in these progenitors ceased prior to $z = 0$ due to their accretion onto the Milky Way, this number of GCs is technically an upper limit. However, for the progenitors in which the youngest GCs on the satellite branch formed, we do not expect the true number to be

much lower – the presence of these young GCs shows that the time of accretion must have been at $z < 1.7$, well after the peak of GC formation activity (Reina-Campos et al. 2018a).

In view of the number of GCs expected per satellite (22^{+5}_{-11}) and the number actually hosted by the satellite branch ($\sim$35), it is most likely that the bulk of the satellite branch was populated by two accreted galaxies of similar mass, which each brought in $\sim$15 GCs. The presence of two such satellites may partially explain the large metallicity spread of the satellite branch. However, we cannot identify a metallicity bimodality in this branch, implying that it is impossible to distinguish between the satellites. We therefore assign the same properties to 'Satellite 1' and 'Satellite 2' across the redshift range $z = 1.7$–6. Finally, at the low end of the mass and metallicity range ($\{\tau/\mathrm{Gyr}, [\mathrm{Fe/H}]\} = \{12, -2\}$), the GCs on the satellite branch extend to considerably lower metallicities than the median metallicity. We associate these with the lowest-mass satellite that we can identify. This 'Satellite 3' can be followed for a rather narrow redshift range using the vectors in Fig. 3, from $z = 3$–6. It may have hosted up to five massive ($M > 10^5\,M_\odot$) GCs, depending on how many GCs at the oldest ages and lowest metallicities are associated with this satellite. For comparison, the expected number based on Fig. 3 is 8^{+3}_{-4}, which is consistent with the number of GCs possibly associated with Satellite 3. For all three identified satellites, the stellar mass growth and metal enrichment histories inferred from Fig. 3 are listed in Table 4.

Fig. 4 visualizes the inferred stellar mass growth histories and metal enrichment histories of the identified progenitors, as well as the merger tree projected in age–mass and age–metallicity space. The rapid assembly of the main progenitor is illustrated by the fact that 10 per cent of its final mass is attained at $z = 2.5$ and 50 per cent at $z = 1.2$. For comparison, the median Milky Way-mass galaxy in the volume-limited sample of 25 E-MOSAICS simulations reaches 50 per cent of its final mass at $z = 0.9$ (Kruijssen et al. 2019). Abundance-matching studies predict that haloes of mass $M_{200} = 10^{12}\,M_\odot$ reach $\{10, 50\}$ per cent of their present-day stellar mass at redshift $z = \{1.9, 0.9\}$ (Behroozi, Wechsler & Conroy 2013; Moster, Naab & White 2013). This rapid mass growth of the Milky Way is also found by comparison to the observed stellar mass growth histories obtained for Milky Way progenitors between redshifts $z = 0.1$–2.5 (grey diamonds in the top panel of Fig. 4 Papovich et al. 2015). At redshifts $1 < z < 2.5$, the Milky Way's stellar mass growth proceeds $\Delta\tau = 0.6$–0.9 Gyr ahead of observed galaxies that are expected to reach the same stellar mass at $z = 0$. This again implies that the Milky Way assembled its stellar mass considerably faster than most galaxies of the same halo mass.

Fig. 4 also shows the basic geometry of the merger tree connecting the four progenitors. Following Table 3, the Milky Way experienced $\sim$9 mergers at $z > 2$, leaving $\sim$6 mergers at $z < 2$ (given its total number of $\sim$15 mergers). Satellites 1 and 2 contain GCs with formation redshifts $z < 2$; hence, they must have been part of the $\sim$6 mergers at $z < 2$. However, their exact time of accretion is unconstrained, as this may have occurred at any time since the formation of the youngest GC on the satellite branch. The accretion time of Satellite 3 is even more poorly constrained based on the age–metallicity distribution only, because it hosts GCs with a narrow range of formation redshifts ($z = 3$–4). Therefore, it may have merged into the main branch at any time $z < 3$. We refine this statement in Section 5.1.

At fixed lookback time or redshift, the identified satellites have stellar masses that are one to two orders of magnitude below the
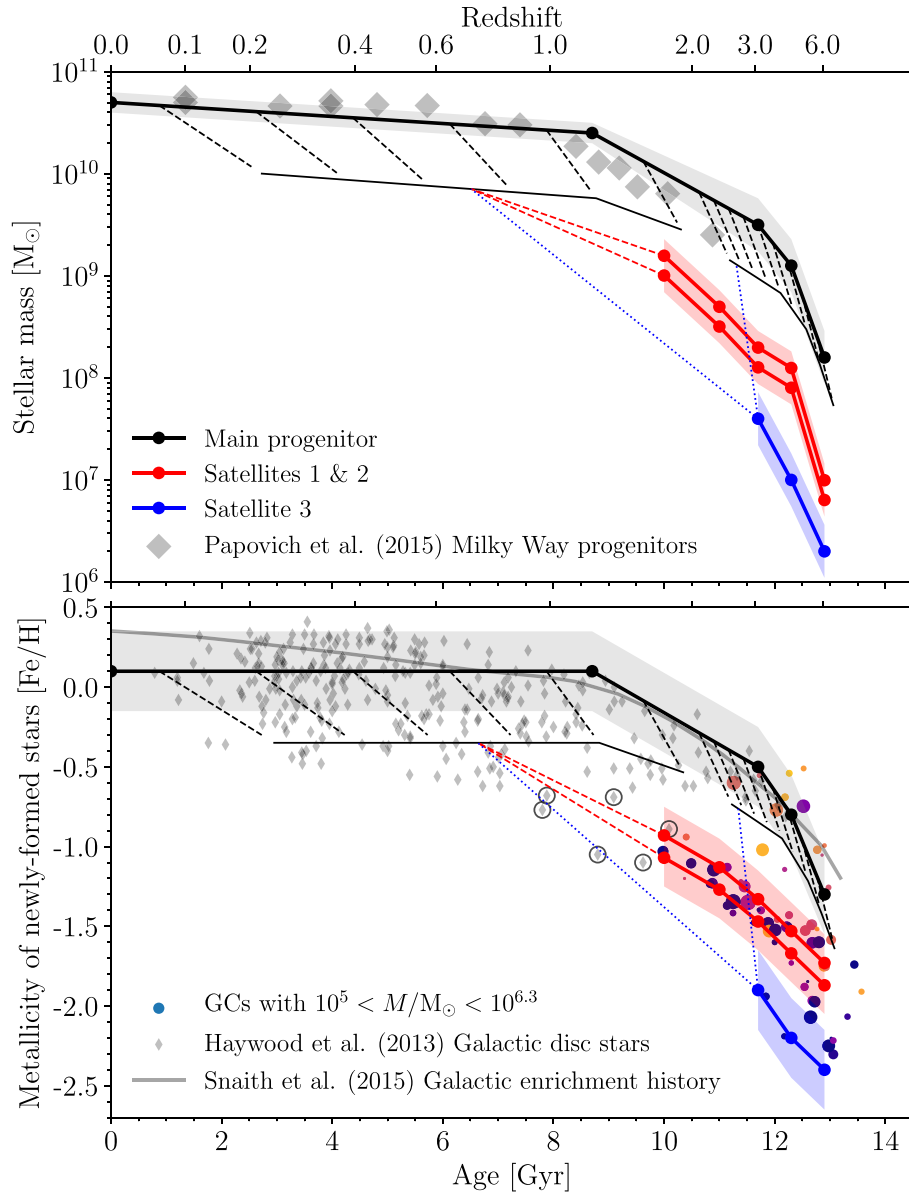
---

in mind. Therefore, we use the Poisson error for upward uncertainties and a factor of 2 as the downward uncertainties on N'_{GC}.

[12]This number includes half of the GCs at the oldest ages and lowest metallicities, where the satellite and main branches merge. In Kruijssen et al. (2019), we show that the GCs in that area of the age–metallicity space are typically equally split between the main progenitor and its satellites.

Figure 4. Stellar mass growth (top panel) and metal enrichment history (bottom panel) of the Milky Way and three of its main satellites, inferred using the observed distribution of the Galactic GC population in age–metallicity space (see Tables 3 and 4). The thick solid lines indicate the progenitors as indicated by the legend in the top panel – to distinguish Satellites 1 and 2, we have added a small vertical offset to the red lines. The shaded areas indicate the uncertainties around the inferred masses and metallicities. Thin lines sketch the topology of the Milky Way's merger tree, projected into age–mass (top) and age–metallicity (bottom) space. These lines have no meaning in terms of mass growth or enrichment and use the information from Table 3 that the Milky Way experienced $N_{\mathrm{br},z>2} \sim 9$ mergers at $z > 2$ and $N_{\mathrm{br}} \sim 15$ mergers in total (implying ~ 6 mergers at $z < 2$). The mergers into the main branch are represented by dashed lines, which are spaced equally over the time intervals $z < 2$ and $z > 2$. Topologically, these mergers are a robust result of our analysis, even if their exact timing within each redshift interval is unknown. The three satellites are connected to the grouped accretion events of both time intervals (thin solid lines) by dashed and dotted lines, with the latter indicating that it is unknown whether Satellite 3 accreted before or after $z = 2$. The large grey diamonds in the top panel show the stellar mass growth histories of Milky Way progenitor galaxies from Papovich et al. (2015), which on average undergo less rapid growth than the Milky Way. For reference, the coloured symbols in the bottom panel match the Galactic GC population in the bottom-right panel of Fig. 1, using the same colour coding of the galactocentric radius. In addition, the small grey diamonds in the bottom panel show the age–metallicity measurements for Galactic disc field stars from Haywood et al. (2013), of which six stars that may have formed in Satellites 1–3 are marked with black circles (see Section 5.1). The grey line represents the fiducial metal enrichment history of Snaith et al. (2015), which is based on the observed star formation history of the Milky Way. This figure demonstrates that the inferred formation and assembly history of the Milky Way is consistent with several independent sets of observational data, revealing that the Galaxy assembled through a combination of rapid *in situ* growth and the accretion of several low-mass ($M_* \sim 10^8$–$10^9 \, \mathrm{M}_\odot$) satellite galaxies.

main branch, with their most recent masses spanning $M_* = 10^8$–$10^9 \, \mathrm{M}_\odot$. Together with the steep main branch in age–metallicity space, this suggests that the Milky Way assembled through a combination of vigorous *in situ* growth and satellite accretion,

without any major mergers since $z \sim 4$. At $z < 4$, any galaxy with a stellar mass comparable to that of the Milky Way's main progenitor (i.e. mass ratio $>1:4$) would have contributed more GCs and at higher metallicities than can be accommodated by the main branch

and the satellite branch of the GC age–metallicity distribution. Due its unstructured nature at higher redshifts, the GC age–metallicity distribution does not enable the identification of major mergers at $z > 4$.

Even though the accretion events of the three satellites onto the main progenitor were only minor mergers, their GC populations do stand out most clearly in Figs 1 and 3. This suggests that the satellites were the most massive to have been accreted by the Milky Way. Lower-mass satellites must have been accreted too, given the expected $N_{br} = 15.1 \pm 3.3$ listed in Table 3, but these likely had such low masses that some of them contributed only a couple of GCs per satellite (∼4 satellites, see Section 5.3), whereas most of them hosted no GCs at all (∼8 satellites).

The bottom panel of Fig. 4 demonstrates that the inferred properties of the Milky Way's progenitors are consistent with several independent observables. First, they trace the age–metallicity distribution of Galactic GCs. This is by construction, but the figure also highlights that the identified progenitors together cover most of the age–metallicity space spanned by the GCs. Secondly, the inferred metal enrichment history of the main progenitor closely matches the age–metallicity distribution of Milky Way disc stars from Haywood et al. (2013), showing that the GCs and field stars in a galaxy follow similar age–metallicity distributions, consistent with our prediction from the E-MOSAICS simulations (Kruijssen et al. 2019).[13] Thirdly, the expected metal enrichment history from the observed star formation history of the Milky Way from Snaith et al. (2015) traces the enrichment history of the main progenitor that we infer from the Galactic GC population nearly perfectly (i.e. within Δ[Fe/H] = 0.1 dex) over the redshift interval $z = 0.4$–4.5. These enrichment histories have been obtained through completely independent methods, implying that their agreement provides an important validation of our results. Finally, even if it is not shown in Fig. 4, the field star age–metallicity relations of the Sagittarius dwarf and the group of GCs formerly associated with Canis Major (both of which have recently been accreted by the Milky Way and possibly correspond to Satellites 2 and 3; see Section 5.1) are consistent with the enrichment histories derived for Satellites 2 and 3 (see e.g. Layden & Sarajedini 2000; Forbes, Strader & Brodie 2004; Siegel et al. 2007). Together, these independent lines of evidence strongly suggest that the properties of the Milky Way's progenitors inferred from their GC population are robust and carry predictive power.

5 DISCUSSION

5.1 Connection of results to known satellites and GCs

We identify three massive ($M_* = 10^8$–10^9 M$_\odot$) satellite progenitors that have been accreted by the Milky Way since $z \sim 3$, based on the properties of the satellite branch in the age–metallicity distribution of Galactic GCs. Several of these GCs are spatially and kinematically associated with known satellites of the Galaxy.[14]
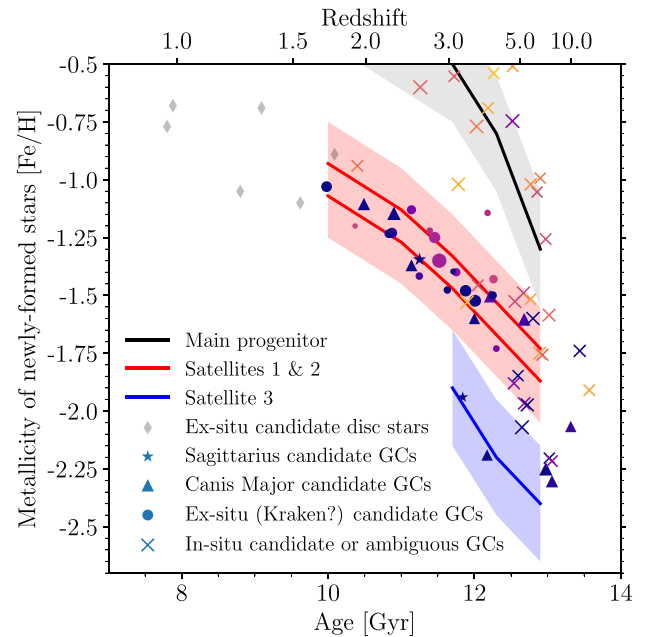

Figure 5. Zoom-in of the age–metallicity distribution of Galactic GCs, highlighting their possible origin. The coloured symbols match the Galactic GC population in the bottom-right panel of Fig. 1, using the same colour coding of the galactocentric radius. However, this time the symbol shape refers to the GCs' origin, as indicated by the legend. In addition, the small grey diamonds indicate the six Galactic disc field stars that may have formed in Satellites 1–3. As in Fig. 4, the solid lines indicate the metal enrichment histories of the progenitors, with shaded areas indicating the uncertainties around the inferred metallicities. This figure illustrates that we expect ∼2 massive ($M > 10^5$ M$_\odot$) GCs to have been brought in by Sagittarius, ∼10 by the 'Canis Major' event, and 10–20 by a new, massive satellite accreted 6–9 Gyr ago, which we name *Kraken*.

The most prominent of these satellites are the Sagittarius dwarf (NGC 5634 and NGC 6715, see Bellazzini et al. 2002; Bellazzini, Ferraro & Ibata 2003; Law & Majewski 2010; Forbes & Bridges 2010) and the GCs formerly associated with the Canis Major 'dwarf' (NGC 1851, NGC 1904, NGC 2808, NGC 4590, NGC 5286, NGC 6205, NGC 6341, NGC 6779, NGC 7078, IC 4499,[15] see Martin et al. 2004; Peñarrubia et al. 2005; Carballo-Bello et al. 2018), which are currently undergoing tidal stripping and accretion onto the Galaxy (Ibata et al. 1994; Majewski et al. 2003; Martin et al. 2004). Fig. 5 shows a zoom-in of the GC age–metallicity distribution from the bottom panel of Fig. 4, highlighting in which (accreted) satellites the GCs may have formed by using different symbol shapes. In this figure, GCs unassociated with any of the satellites (see below) are considered to be ambiguous in terms of

---

[13]The Haywood et al. (2013) field stars reside in the solar neighbourhood, within a distance of ∼100 pc. However, this does not mean these stars formed there. The dynamical redistribution of stars by radial migration (e.g. Sellwood & Binney 2002) or satellite accretion implies that they are expected to have originated from a variety of environments. This has no implications for the comparison in Fig. 4, as we merely include the stellar sample with the goal of comparing the enrichment histories of the Milky Way's progenitors inferred from its GCs to a typical field star sample that currently resides in the Galactic disc.

[14]Recall that we restrict our analysis to GCs with masses $M > 10^5$ M$_\odot$.

[15]The inclusion of several of these GCs hinges on their association with the Monoceros stream, which Martin et al. (2004) proposed is the tidal debris of a dwarf galaxy named Canis Major. However, the current consensus is that the Canis Major dwarf never existed (see Peñarrubia et al. 2005; de Boer, Belokurov & Koposov 2018; Deason, Belokurov & Koposov 2018b; and Carballo-Bello et al. 2018 for discussions). We do note that all of these GCs except NGC 4590, NGC 7078, and IC 4499 have highly similar apocentre distances, pericentre distances, eccentricities, and angular momenta (Gaia Collaboration 2018a; Sohn et al. 2018). For historical reasons, we therefore maintain the nomenclature of referring to one of the identified progenitor satellites as Canis Major, but acknowledge that the associated GCs were brought in by a different progenitor.

having an *in situ* or *ex situ* origin. In addition, GCs with metallicities [Fe/H] $> 2 - 0.25\tau/\mathrm{Gyr}$ are considered to have formed *in situ*, unless they have been spatially or kinematically associated with a satellite in the literature. The field star age–metallicity relation of Sagittarius connects directly to the satellite branch of the GC age–metallicity distribution, albeit to the lower end of its metallicity range (e.g. Layden & Sarajedini 2000; Siegel et al. 2007), and the old open cluster population of the 'Canis Major' GCs is a natural continuation of the satellite branch towards younger ages and higher metallicities (Forbes et al. 2004). It is therefore plausible that one of the identified satellites represents Sagittarius and another corresponds to the galaxy that contributed the 'Canis Major' GCs.

Based on the number of associated GCs, we expect Sagittarius to have been the least massive of the above two known accreted satellites. In the age–metallicity distribution of Galactic GCs shown in Fig. 5, NGC 5634 ($\{\tau/\mathrm{Gyr}, [\mathrm{Fe/H}]\} = \{11.84 \pm 0.51, -1.94\}$) is associated with Satellite 3. Due to its high metallicity, NGC 6715 ($\{\tau/\mathrm{Gyr}, [\mathrm{Fe/H}]\} = \{11.25 \pm 0.59, -1.34\}$) resides in the main satellite branch and thus coincides with Satellites 1 and 2 in age–metallicity space. However, this GC most likely represents the nuclear cluster of Sagittarius, implying an extended star formation history and a wide metallicity distribution, extending down to [Fe/H] $= -1.9$ (Carretta et al. 2010). This lower bound makes NGC 6715 a natural extension of the Satellite 3 age–metallicity track. Also in terms of its number of massive GCs ($N_{\mathrm{GC}} \gtrsim 2$) and its estimated total number of GCs ($N_{\mathrm{GC}} = 5\text{--}10$, Law & Majewski 2010), Sagittarius is likely to have represented the lowest-mass progenitor among the three that we identified, for which we estimate $N_{\mathrm{GC}} = 8^{+3}_{-4}$ had it evolved to $z = 0$ without being disrupted. This match is corroborated by Sagittarius' estimated stellar mass prior to accretion onto the Milky Way, which is several $10^8 \, \mathrm{M}_\odot$ (e.g. Niederste-Ostholt et al. 2010; Niederste-Ostholt, Belokurov & Evans 2012). Our predicted early ($z \geq 3$) stellar mass growth and metal enrichment history is also consistent with these findings – with a mass and metallicity of $M_* = 4 \times 10^7 \, \mathrm{M}_\odot$ and [Fe/H] $= -1.9$ at $z = 3$, Satellite 3 is expected to reach a mass of $M_* \sim 2 \times 10^8 \, \mathrm{M}_\odot$ at $z = 1$ (e.g. Moster et al. 2013; Behroozi et al. 2013), with an expected metallicity of [Fe/H] $= -0.9$ (e.g. Forbes & Bridges 2010). This projected metallicity is Δ[Fe/H] ~ 0.3 dex lower than the metallicity of the young ($\tau = 3\text{--}8 \, \mathrm{Gyr}$), low-mass ($M < 10^5 \, \mathrm{M}_\odot$) GC population of Sagittarius (Law & Majewski 2010), confirming the known result that Sagittarius has a current metallicity higher than expected for its relatively low mass (e.g. Martínez-Delgado et al. 2005). In view of these results, it is likely that Satellite 3 is the Sagittarius dwarf.

Progenitors more massive than Sagittarius are required for having populated the satellite branch of the Milky Way's GC age–metallicity distribution. As discussed above, we predict the existence of two such progenitors, dubbed Satellite 1 and 2. With its substantial population of 5–10 potential, massive GCs, the galaxy that contributed the 'Canis Major' GCs is the obvious candidate for representing one of these satellites. Fig. 5 shows that all 'Canis Major' GCs with formation redshifts $z \leq 6$ (or $\tau > 12.9 \, \mathrm{Gyr}$) match the age–metallicity track of Satellites 1 and 2. Contrary to Sagittarius, its putative nuclear cluster NGC 2808 (Forbes & Bridges 2010; Carballo-Bello et al. 2018) does not have a metallicity spread (Carretta 2015) and as a result it traces the age–metallicity evolution of its host at $\{\tau/\mathrm{Gyr}, [\mathrm{Fe/H}]\} = \{10.90 \pm 0.57, -1.14\}$. The expected number of massive GCs ($N_{\mathrm{GC}} = 22^{+5}_{-11}$) provides a good match to the observed number, provided that we missed one or two associated GCs that should be added to the 10 'Canis Major' GCs. In terms of its stellar mass prior to accretion onto the

Milky Way, Peñarrubia et al. (2005) obtain $M_* = 6 \pm 3 \times 10^8 \, \mathrm{M}_\odot$, with the caveat that the mass is poorly constrained and could be as high as $M_* = 2 \times 10^9 \, \mathrm{M}_\odot$. Such a high mass would be consistent with the mass evolution we estimate for Satellites 1 and 2, reaching $M_* = 1.3 \times 10^9 \, \mathrm{M}_\odot$ at $z = 1.7$. Their metallicity at that redshift is [Fe/H] $= -1.0$, which is expected to evolve to [Fe/H] $= \{-0.8, -0.5\}$ at $z = \{1, 0.5\}$ (Forbes & Bridges 2010). These metallicities provide an excellent match to those of the old open clusters associated with the 'Canis Major' GCs, which are [Fe/H] $= -0.45$ (Forbes et al. 2004). Together, Sagittarius and the 'Canis Major' event represent the minority of GCs on the satellite branch, making it likely that the latter is the less massive of Satellites 1 and 2. We therefore associate the galaxy contributing the 'Canis Major' GCs with Satellite 2.

Based on their ages ($\tau < 12.5 \, \mathrm{Gyr}$), metallicities ([Fe/H] $< 2 - 0.25\tau/\mathrm{Gyr}$, which gives [Fe/H] $< \{-0.5, -1.0\}$ at $\tau = \{10, 12\} \, \mathrm{Gyr}$), and galactocentric radii ($R > 5 \, \mathrm{kpc}$), there are 18 further GCs associated with the satellite branch of the GC age–metallicity distribution in Fig. 5.[16] These are NGC 362, NGC 1261, NGC 3201, NGC 5139, NGC 5272, NGC 5897, NGC 5904, NGC 5946, NGC 6121, NGC 6284, NGC 6544, NGC 6584, NGC 6752, NGC 6864, NGC 6934, NGC 6981, NGC 7006, and NGC 7089. While some of the oldest of these GCs may have formed *in situ*, we expect a large fraction of them to have been accreted. Six of these GCs (NGC 362, NGC 3201, NGC 5139, NGC 6121, NGC 6934, NGC 7089) have retrograde orbits (see Dinescu, Girard & van Altena 1999; Allen, Moreno & Pichardo 2006; although both studies do not agree on each of these GCs individually), whereas the others do not. In general, these GCs have a variety of orbital kinematics. This suggests the existence of more than one progenitor (of which the retrograde one likely had NGC 5139/ω Cen as its nuclear cluster; cf. Bekki & Freeman 2003), but the lack of structure in the satellite branch does not enable us to distinguish these.

In view of the above discussion, we refrain from associating individual GCs with Satellite 1, but encourage future studies to look for phase-space correlations between the above set of GCs and those that have been proposed to be associated with Sagittarius or the 'Canis Major' event (e.g. using *Gaia*, Gaia Collaboration 2016a). As such, the above GCs represent a 'wish list' of interesting targets for kinematic follow-up work. This will enable identifying which of them belong to the inferred Milky Way progenitors. This may include GCs of which the age has not been measured to date, as the identified progenitors have sufficiently high masses to have hosted additional GCs. Such efforts may also identify groups of GCs originating from other accreted satellites, in addition to the three that are specifically identified in this work. After all, we estimate a total number of $N_{\mathrm{br}} = 15.1 \pm 3.3$ accreted satellites, of which about half likely brought in GCs (see Section 5.3).

Similarly, we identify six disc stars from the Haywood et al. (2013) sample in Fig. 4 that have metallicities [Fe/H] < -0.65 and ages $\tau < 11 \, \mathrm{Gyr}$, making them a natural extension of the GC satellite branch. If this interpretation is correct, it leads to the plausible conclusion that at least one of the satellites continued forming field stars after its youngest GC and accreted at $z < 1$. If the satellite was accreted already at larger redshifts, the stars likely formed in the MW from the gas brought in by the satellite. In both cases, their origin is linked to satellite accretion. These

---

[16] A small number of GCs with ages $\tau > 12.5 \, \mathrm{Gyr}$ or galactocentric radii $R < 5 \, \mathrm{kpc}$ may still have an *ex situ* origin, but we deliberately adopt conservative sample limits.

stars are also shown in Fig. 5 and are all part of the *Hipparcos* catalogue, with identifiers HIP 36640, HIP 54641, HIP 57360, HIP 77637, HIP 80611, and HIP 102046. All six stars are part of the second *Gaia* data release (DR2, Gaia Collaboration 2018b), listing high-precision positions, parallaxes, radial velocities, and proper motions. This provides the information necessary to verify if these stars are kinematically associated with the above candidate GCs and with (the remnant streams of) Sagittarius, the galaxy contributing the 'Canis Major' GCs, or Satellite 1.

Satellite 1 remains unassociated with any known satellites of the Milky Way or their tidal debris. Therefore, it is likely to have been accreted several Gyr ago. Deason et al. (2013, also see Pillepich et al. 2014) suggest that the break in the density profile of the Galactic stellar halo at $R \sim 25$ kpc (e.g. Watkins et al. 2009; Sesar, Jurić & Ivezić 2011) indicates an accretion event some 6–9 Gyr ago (corresponding to $z = 0.6$–1.3) of a single satellite that was considerably more massive than other accreted satellites. This finding is supported by independent evidence from halo kinematics (Belokurov et al. 2018; Deason et al. 2018a). In the context of Fig. 4, it is natural to propose that this event corresponds to the accretion of Satellite 1, which would have had a mass of $M_* \sim 2 \times 10^9 \, \mathrm{M_\odot}$ at that time. Interestingly, the median galactocentric radius of the 18 candidate GCs associated with Satellite 1 listed above is ~ 8 kpc, which is considerably smaller than the nucleus of Sagittarius (NGC 6715, ~ 19 kpc, Harris 1996) and also smaller than the putative nucleus of the galaxy contributing the 'Canis Major' GCs (NGC 2808, ~ 11 kpc, Harris 1996). This suggests that these GCs were brought in by a massive progenitor that spiralled in farther due to dynamical friction than any other satellite. The results of this paper show that the echo of this satellite's existence is not only present in the density profile and kinematics of the stellar halo, but can also be seen in the age–metallicity distribution of Galactic GCs. Acknowledging the enigmatic nature of this satellite, which was plausibly the most massive satellite ever to have merged with the Milky Way, we propose to name it *Kraken*, after the elusive giant sea monsters that were rumoured to sink ships many centuries ago.

5.2 The relative contributions of *in situ* and *ex situ* GCs

Following on from the above discussion, we can use the inferred assembly history of the Milky Way to determine the part of the GC population that formed *in situ* and *ex situ*. The Milky Way has 91 GCs with $M > 10^5 \, \mathrm{M_\odot}$ (using $M_{V,\odot} = 4.83$ and $M/L_V = 2 \, \mathrm{M_\odot} \, \mathrm{L_\odot^{-1}}$, Harris 1996, 2010 edition). This agrees with the number of GCs expected to be present in the main progenitor at $z = 0$ from Table 4 ($N'_{\mathrm{GC}} = 150^{+12}_{-75}$), but also shows that the Milky Way is at the low end of the expected range, possibly due to a lack of mergers with GC-rich galaxies. Out of these 91 GCs, 86 per cent have $[\mathrm{Fe/H}] < -0.5$, for which Fig. 5 shows that about 50 per cent are associated with the satellite branch.[17] If we make the plausible assumption that the GCs at $[\mathrm{Fe/H}] > -0.5$ formed *in situ*, this implies that about 43 per cent of the Galactic GCs have an *ex situ* origin, i.e. 39 out of the 91 massive GCs come from accreted satellites, whereas the remaining 52 out of 91 formed in the main progenitor. In the absence of further evidence, it is reasonable to assume the same fractions apply to GCs with $M < 10^5 \, \mathrm{M_\odot}$. For a total population of 157 Galactic GCs in the Harris (1996, 2010

edition) catalogue, we thus expect 67 with an *ex situ* origin and predict that 90 formed *in situ*.

Unsurprisingly, the fraction of GCs with an *ex situ* origin depends on the metallicity. The *ex situ* fraction must approach zero at high metallicities ($[\mathrm{Fe/H}] > -0.5$), because the Milky Way has not accreted any satellites sufficiently massive to provide such metal-rich GCs (see Section 5 and e.g. Mackey & Gilmore 2004), but it increases towards low metallicities. We do not expect the *ex situ* fraction to reach unity at any metallicity – even at the lowest metallicities, a significant fraction of the metal-poor GCs should have formed *in situ* during the early enrichment of the main progenitor of the Milky Way. For the E-MOSAICS galaxies, about 50 per cent of the GCs with metallicities $[\mathrm{Fe/H}] < -1.5$ typically formed *in situ* (see figs. 8 and 9 of Kruijssen et al. 2019). For the Milky Way, $\{25, 50\}$ per cent of the GCs with $[\mathrm{Fe/H}] < -1.5$ are contained within a galactocentric radius of $R < \{5, 10\}$ kpc, which suggests that many of these GCs also have an *in situ* origin (compare figs. 2 and 8 of Kruijssen et al. 2019). This conclusion differs from previous work, which often assumes an *ex situ* origin for all metal-poor GCs not showing disc-like kinematics and chemistries (e.g. Leaman et al. 2013).

5.3 Comparison to other constraints on the formation and assembly of the Milky Way

Our constraints on the Milky Way's assembly and accretion history are consistent with a variety other studies, but we also find important differences relative to (and extensions of) previous results. The total stellar mass growth history integrated over all progenitors matches the observed star formation history of the Milky Way, with 50 per cent of its stars predicted to have formed at $\tau_\mathrm{f} = 10.1 \pm 1.4$ Gyr and the observed star formation history reaching this point at $\tau_\mathrm{f} = 10.5 \pm 1.5$ Gyr (Snaith et al. 2014). The same applies to the inferred metal enrichment history of the main progenitor, which provides an excellent match to the age–metallicity distribution of the thick-disc field stars (Haywood et al. 2013) and to the enrichment history derived from the star formation history (Snaith et al. 2015).

Overall, our results imply that the Milky Way must have formed very rapidly in comparison to galaxies of similar masses. This conclusion stems from our comparisons to the suite of 25 E-MOSAICS galaxies (see Section 4.1), to the halo mass growth histories predicted by the extended Press–Schechter formalism (Correa et al. 2015, see Section 4.1), to stellar mass growth histories expected from abundance matching (Behroozi et al. 2013; Moster et al. 2013; see Section4.2), and to the observed stellar mass growth history of Milky Way progenitors across cosmic time (see Fig. 4; Papovich et al. 2015). In addition, our conclusion of the rapid assembly of the Milky Way is supported by the findings of Mackereth et al. (2018), who show that the presence of a bimodal $[\alpha/\mathrm{Fe}]$ distribution of the Galactic disc field stars is a rare feature among Milky Way-mass galaxies in EAGLE, indicating an early phase of vigorous gas accretion and rapid star formation. These results all show that the formation and assembly history of the Milky Way is atypical for $L^\star$ galaxies.[18]

The agreement with previous findings also extends to the satellite progenitors. For instance, Deason, Belokurov & Weisz (2015) and

---

[17]Based on sect. 5.1 of Kruijssen et al. (2019), this estimate includes half of the 'ambiguous' GCs, i.e. the crosses in Fig. 5 with $[\mathrm{Fe/H}] < 2 - 0.25\tau/\mathrm{Gyr}$.

[18]An immediate implication of this result is that simulations of 'typical' Milky Way-mass galaxies are unlikely to reproduce the properties of the Galactic GC population, unless the adopted GC formation and evolution model is missing critical physical ingredients.

Deason, Mao & Wechsler ([2016](#)) show that the accreted stellar mass of Milky Way-mass galaxies is mostly supplied by massive satellites, covering the stellar mass range $M_* = 10^8$–$10^{10}\,M_\odot$, or $M_* = 10^8$–$10^9\,M_\odot$ for galaxies with a relatively quiescent merger history such as the Milky Way. This mass range agrees very well with the expected masses of Satellites 1–3 prior to their accretion, which in Section 5.1 are inferred to range from a few 10^8 to $2 \times 10^9\,M_\odot$. Given that these most massive satellites merged late (at $z < 2$, see Section 5.1), our comparison of the satellite progenitor population ($M_* < 2 \times 10^8\,M_\odot$) with the stellar mass growth history of the main progenitor in Section 4.2 shows that the Milky Way did not experience any major mergers (i.e. those with stellar mass ratios $>1{:}4$) since $z \sim 4$ (corresponding to the past $\sim$12.3 Gyr). This extends previous literature constraints, which ruled out major mergers at $z \lesssim 2$ (i.e. the past $\sim$10.5 Gyr; see e.g. Wyse [2001](#); Hammer et al. [2007](#); Stewart et al. [2008](#); Shen et al. [2010](#); Bland-Hawthorn & Gerhard [2016](#)). We also find that several of the satellites underwent (possibly major) mergers prior to their accretion onto the Milky Way, because the total number of progenitors ($N_{\rm leaf} = 24.1 \pm 10.2$) exceeds the number of mergers or accretion events experienced by the Milky Way ($N_{\rm br} = 15.1 \pm 3.3$), even if the former carries a considerable uncertainty. It is not unusual for accreted satellites to have undergone previous merging – Deason, Wetzel & Garrison-Kimmel ([2014](#)) predict that about one-third of all dwarf galaxies within the virial radius experienced a major (defined in their study as having a stellar mass ratio $>1{:}10$, whereas we use $>1{:}4$) merger since $z \sim 4$ (also see e.g. Amorisco, Evans & van de Ven [2014](#)).

The inferred total number of $\sim$15 accretion events exceeds the number of 7 accretion events of satellites hosting GCs obtained by Mackey & Gilmore ([2004](#)), illustrating that only about half of the Milky Way's progenitors hosted GCs. Indeed, Mackey & Gilmore ([2004](#)) suggest that 6–11 progenitors may not have hosted any GCs, which implies a total of 13–18 mergers and exactly matches our estimate of $N_{\rm br} = 15.1 \pm 3.3$.[19] If we adopt the observed relation between the total GC population mass and the host galaxy's halo mass (e.g. Blakeslee [1997](#); Spitler & Forbes [2009](#); Durrell et al. [2014](#); Harris et al. [2017](#)) and assume a typical GC mass of $M = 2 \times 10^5\,M_\odot$, this requires that about half of the accreted satellites had halo masses $M_{200} \lesssim 10^{10}\,M_\odot$ (which have $N_{\rm GC} < 1$), corresponding to stellar masses $M_* \lesssim 2 \times 10^7\,M_\odot$ (e.g. Behroozi et al. [2013](#); Moster et al. [2013](#)). The remaining, massive progenitors span the mass range $M_* = 2 \times 10^7$–$2 \times 10^9\,M_\odot$, with the three most massive progenitors corresponding to Satellites 1–3 identified here, i.e. Sagittarius, the galaxy contributing the 'Canis Major' GCs, and Kraken. The prediction that Kraken, the most massive satellite, was accreted 6–9 Gyr ago is also consistent with the idea that satellites surviving to $z = 0$ are less massive than the previously disrupted ones (Sales et al. [2007](#)). This emphasizes the point that the GC population of the Milky Way's current satellite system is not necessarily representative for the complete *ex situ* population.

With a typical mass scale of $M_* \sim 2 \times 10^8\,M_\odot$ and a range around this mass scale of two orders of magnitude ($M_* = 2 \times 10^7$–$2 \times 10^9\,M_\odot$), the inferred GC-bearing progenitors cover a narrower mass range and have higher masses than proposed by Leaman et al.

([2013](#)) based on the Galactic GC age–metallicity distribution. These authors find masses in the range $M_* = 3 \times 10^5$–$10^9\,M_\odot$, with a typical mass scale of $M_* \sim 3 \times 10^7\,M_\odot$. The difference is largely caused by the fact that Leaman et al. ([2013](#)) associate all old, metal-poor GCs with (predominantly low-mass) satellites, whereas we consider a large fraction of these to have formed in the precursors of the Milky Way's main progenitor and its most massive accreted satellites. The latter interpretation is more consistent with the other observational constraints on the formation and assembly of the Milky Way discussed above. An additional source of discrepancy may be that there exists some tension (of $\Delta{\rm [Fe/H]} \sim 0.3$) between the observed galaxy mass–metallicity relation and that produced by the EAGLE Recal-L025N0752 simulation at galaxy masses $M_* < 10^9\,M_\odot$ (fig. 13 Schaye et al. [2015](#)). This is not necessarily an intrinsic bias of EAGLE, as nucleosynthetic yields and metallicity calibrations are uncertain at a similar level (Schaye et al. [2015](#)). Irrespective of the reason, if the simulations systematically overestimate the metallicities of low-mass galaxies, then this would lead to a corresponding overprediction by a factor of several of the satellite progenitor masses reported here. The work by Leaman et al. ([2013](#)) uses empirical age–metallicity relations of satellite galaxies in the Local Group to estimate satellite progenitor masses. These carry an uncertainty of a similar magnitude due to the choice of metallicity calibration, but this is independent of any bias possibly present in EAGLE.

Following from the inferred formation and assembly history of the Milky Way, we estimate that 67 out of the 157 Galactic GCs from the Harris ([1996](#), 2010 edition) catalogue (i.e. a little more than 40 per cent) have an *ex situ* origin. This is higher than the number derived by Mackey & Gilmore ([2004](#), 40 *ex situ* GCs) based on a comparison of the core radii of Galactic GCs to those of GCs in dwarf galaxies. However, the difference is largely caused by our inclusion of about half of the old, metal-poor GCs in the part of the GC age–metallicity distribution where the satellite branch is indistinguishable from the main branch. This choice is motivated by the ex situ fractions obtained for this part of the age–metallicity space in the E-MOSAICS galaxies (Kruijssen et al. [2019](#)) and is not necessarily inconsistent with the idea from Mackey & Gilmore ([2004](#)) that inflated GC core radii trace the *ex situ* origin of GCs – if the natal dwarf galaxies of the oldest GCs were accreted by the Milky Way during its initial collapse at $z > 4$, then the properties of these satellites and the Milky Way's main progenitor at that time may have been similar, resulting in similar core radii. As such, the estimated number of Galactic GCs formed *ex situ* from Mackey & Gilmore ([2004](#)) is a lower limit.

By combining the observed fraction of dwarf galaxies hosting nuclear clusters with the satellite progenitor statistics derived here, we can also make an estimate of the number of former nuclear clusters among the Galactic GC population. Across the galaxy mass range of the GC-bearing progenitors considered here ($M_* = 2 \times 10^7$–$2 \times 10^9\,M_\odot$), a fraction $f_{\rm N} \approx 0.65$ of dwarf galaxies in the Fornax Cluster host nuclear clusters (Muñoz et al. [2015](#); Ordenes-Briceño et al. [2018](#)), whereas $f_{\rm N} \approx 0.15$ for the remaining progenitors ($M_* = 4.5 \times 10^6$–$2 \times 10^7\,M_\odot$). If the same applies to the progenitors of the Milky Way and all nuclear clusters survived the accretion and tidal disruption of their host, then the roughly equal estimated number of progenitors among these two mass bins implies a mean nucleation fraction of $f_{\rm N} \approx 0.4$ across the $N_{\rm br} = 15.1 \pm 3.3$ progenitors of the Milky Way. Based on these numbers, we predict that the Galactic GC population hosts $N_{\rm nucl} = 6.0 \pm 1.3$ former nuclear clusters, which is similar to the number of Galactic GCs for which this has been proposed in the observational literature (see

---

[19] In order to match the total mass of the stellar halo, Mackey & Gilmore ([2004](#)) do assume lower satellite masses than those of our inferred progenitors, with a typical mass scale in logarithmic mass space of $10^{7.8}\,M_\odot$ as opposed to our $10^{8.3}\,M_\odot$. However, as we will see below, a substantial fraction of accretion events contribute to the Galactic (thick) disc and bulge, implying that such low satellite masses are not required.

e.g. sect. 4.1 of Pfeffer et al. 2014 for a discussion). These 'GCs' are likely to exhibit spreads in [Fe/H] and possibly age.

Finally, the satellite progenitors of the Milky Way identified in this paper imply a total accreted mass of $M_* \sim 3$–$4 \times 10^9 \, \mathrm{M}_\odot$. Naively, this may seem to violate the (smaller) total mass of the Galactic stellar halo ($10^9 \, \mathrm{M}_\odot$, e.g. Freeman & Bland-Hawthorn 2002). However, it is likely these masses are consistent, because not all of the accreted mass has been deposited in the halo. For instance, the galaxy contributing the 'Canis Major' GCs ($\sim 10^9 \, \mathrm{M}_\odot$) may largely have deposited stars in the thick disc (Martin et al. 2004), whereas the central spheroids of other dwarfs are likely to survive tidal stripping and eventually spiral in due to dynamical friction, thus merging with the Galactic disc or bulge and depositing a large fraction of their stellar mass there (e.g. Meza et al. 2005; Amorisco 2017).

5.4 Dependence of results on the absolute GC age calibration

The main caveat of the presented analysis is posed by the large uncertainties on the age measurements of GCs. This does not as much affect their relative age differences,[20] but the absolute (or 'reference') GC age hinges critically on the GC age calibration. Due to these uncertainties, many observational studies focus on relative ages (e.g. Marín-Franch et al. 2009; Wagner-Kaiser et al. 2017). Given that the ages of the Galactic GCs lean towards the highest redshifts at which stars of the corresponding metallicities are formed in the 25 Mpc EAGLE Recal-L025N0752 volume (see Fig. 3), we expect that any systematic offset in the absolute ages is one that would have caused them to be overestimated.

If the absolute ages of Galactic GCs were smaller than listed in the three adopted literature catalogues (Forbes & Bridges 2010; Dotter et al. 2010; Dotter et al. 2011; VandenBerg et al. 2013) and our combined mean sample (Appendix A), then this has several implications for the derived formation and assembly history of the Milky Way. First (and trivially), the Galaxy would not have undergone as rapid mass growth and metal enrichment as the data currently require. Secondly, the quantities derived from the median age $\widetilde{\tau}$ and the GC metal enrichment rate $\mathrm{d}[\mathrm{Fe/H}]/\mathrm{d}\log t$ (see Table 3) would be biased towards lower values (they all correlate positively with these two age-based metrics). Thirdly, the number of GCs per halo derived from the bottom panel of Fig. 3 would decrease, such that the Galactic GC population would be assembled from a larger number of progenitors. In general, each of these implications of a shift towards younger ages results in a more gradual formation and assembly of the Milky Way, with a richer merger tree and $\gg 3$ satellite progenitors that should be associated with the satellite branch in the GC age–metallicity distribution.

Importantly, a downward revision of the observed GC ages would lead to a number of problems. First, many of the galaxy-related quantities in Table 3 are obtained from more than one GC-related metric, which provides a useful consistency check. Quantities derived from absolute GC ages ($\widetilde{\tau}$ and $\mathrm{d}[\mathrm{Fe/H}]/\mathrm{d}\log t$) are currently consistent with those that are estimated using other, independent metrics. Secondly, it would be hard to reproduce the well-defined nature of the satellite branch in Fig. 3 with a large number of satellite progenitors. Especially at the (even lower) required masses, the progenitors would be expected to form stars at a considerably

wider range of metallicities at a given redshift. Otherwise, it would be highly coincidental that all of these progenitors had identical metal enrichment histories. Finally, the results obtained from our GC-based analysis are found to be consistent with independent measurements from the literature, such as the star formation history, metal enrichment history, and field star ages and metallicities, both for the Galactic disc and for the 'Canis Major' and Sagittarius dwarfs. Together, these considerations argue against a significant systematic bias of the GC ages.

Finally, we note that our results are insensitive to differences in the absolute GC age calibration *between* the three literature samples used. For the subset of 36 GCs with masses $M > 10^5 \, \mathrm{M}_\odot$ and metallicities $-2.5 < [\mathrm{Fe/H}] < -0.5$ that appear in each of these samples, the median ages from the Forbes & Bridges (2010), Dotter et al. (2010, 2011), and VandenBerg et al. (2013) catalogues are $\overline{\tau} = \{12.26, 12.75, 12.01\}$ Gyr, respectively. These mean ages agree to within the age uncertainties listed in Appendix A, showing that the adopted uncertainties already reflect any possible biases. If we change the median age $\widetilde{\tau}$ of the Galactic GCs by a nominal $\Delta\tau = 0.5$ Gyr, each of the derived quantities describing the Milky Way's formation and assembly history in Table 3 changes by less than the quoted uncertainty. This insensitivity to any biases in GC age arises because the relations used for inferring these quantities exhibit a scatter that is similar in magnitude to the slope of the relation in units of Gyr^{-1} (see table 7 of Kruijssen et al. 2019). This means that a systematic age bias in excess of 1 Gyr is needed to significantly change the results. The same applies to the other quantities that could be sensitive to the absolute age calibration, such as $\mathrm{d}[\mathrm{Fe/H}]/\mathrm{d}\log t$. Because the GC ages that have been measured since 2001 agree to within 5–10 per cent (i.e. < 1 Gyr; Dotter 2013), we conclude that our results are robust against systematic age uncertainties, unless all GC age measurements share the same systematic bias.

Further improvement of the GC age uncertainties may be achieved using highly accurate distances to reference stars that can be obtained with *Gaia* (Gaia Collaboration 2016a,b). However, the measurements of chemical abundances will remain a major uncertainty for the foreseeable future. There exist systematic differences in metallicity and abundance scales adopted by various studies reporting GC ages (e.g. Carretta & Gratton 1997; Kraft & Ivans 2003; Carretta et al. 2009), which in turn affect the GC age measurements (e.g. VandenBerg, Denissenkov & Catelan 2016).[21] These may be improved by better measurements of the stellar mass–luminosity relation, which is constrained by studies of eclipsing binaries (e.g. Henry & McCarthy 1993; Malkov 2007). The main obstacle for applying these constraints to GCs is that they exhibit internal spreads in helium abundance (e.g. Bastian & Lardo 2018), which in turn modify the stellar mass–luminosity relation (e.g. Salaris et al. 2006; VandenBerg et al. 2014; Chantereau, Charbonnel & Meynet 2016). Given the major importance of accurate GC ages for reconstructing the formation and assembly history of the Milky Way and potentially other galaxies, we stress the importance of continued work on these issues.

---

[20]This is illustrated by the considerable structure in age–metallicity space (see e.g. Fig. 1), which would have been washed out if the relative ages were uncertain.

[21]As shown by VandenBerg et al. (2013), uncertainties in the metallicity scale mainly affect the ages derived for metal-rich GCs ([Fe/H] > -0.7) by Marín-Franch et al. (2009). Our conclusions do not change when accounting for this source of uncertainty, because we omit GCs with [Fe/H] > -0.5 and average over three different GC age–metallicity samples (of which the ages from Marín-Franch et al. 2009 are contained in the Forbes & Bridges 2010 compilation).

5.5 Dependence of results on the adopted GC model

An additional caveat may come from the physical model used to calculate the formation and disruption of the GCs in E-MOSAICS. Specifically, we use physical prescriptions for the cluster formation efficiency and the (high-mass end of the) initial cluster mass function, as well as for GC mass loss due to the local tidal field that they experience in the simulations. If these prescriptions are incorrect, in terms of either their absolute values or their environmental scaling, then this may bias the GC age–metallicity distribution.

The fundamental approach of E-MOSAICS is to investigate whether the observed properties of GC populations can be reproduced when assuming that they formed according to local-Universe physics. The prescriptions for the cluster formation efficiency, initial cluster mass function, and cluster disruption, as well as their environmental dependence have all been extensively tested against observations of stellar cluster populations in nearby galaxies, to the point that they accurately describe the observations to within < 0.3 dex. In Pfeffer et al. (2018), Reina-Campos et al. (2018a), Usher et al. (2018), and Pfeffer et al. (in prep.), we show that switching off the environmental dependences of the cluster formation efficiency and the (high-mass end of the) initial cluster mass function results in young cluster populations and GC populations that are inconsistent with observations in terms of their spatial distributions, formation histories, mass–metallicity distributions, luminosity functions, and age distributions. In addition, the restriction of the analysed GC sample to those with $M > 10^5 \, \mathrm{M_\odot}$ minimizes any influence of GC disruption, which mostly affects GCs of lower masses (also see Kruijssen et al. 2019; Reina-Campos et al. 2018b). These points suggest that the uncertainties introduced by the adopted GC formation and disruption model are minor compared to the age uncertainties discussed in Section 5.4.

6 SUMMARY AND IMPLICATIONS

In this paper, we have reconstructed the formation and assembly history of the Milky Way using the age–metallicity distribution of its GC population. To achieve this, we have used the results of the E-MOSAICS project, which is a volume-limited suite of 25 cosmological hydrodynamical zoom-in simulations of Milky Way-mass galaxies that includes a self-consistent model for the formation and disruption of stellar cluster populations (Pfeffer et al. 2018; Kruijssen et al. 2019), and applied these to a compilation of ages and metallicities of 96 Galactic GCs (see Appendix A). Using the GC age–metallicity distribution and its correlation with the host galaxy's formation and assembly history (see Kruijssen et al. 2019), we derive 12 different quantities describing the Milky Way's mass growth history, its metal enrichment history, and its merger tree. These results show that, in terms of its integrated properties, the Milky Way falls close to the median of the E-MOSAICS galaxies. However, in terms of quantities describing its growth, assembly, and metal enrichment rate, the Milky Way is highly unusual, spanning the 72th–94th percentile of the E-MOSAICS simulations. This shows that the Milky Way formed extremely rapidly, which we quantify by comparing our results to the halo mass growth histories predicted by the extended Press–Schechter formalism (Correa et al. 2015), to the stellar mass growth histories expected from abundance matching (Behroozi et al. 2013; Moster et al. 2013), and to the observed stellar mass growth history of Milky Way progenitors across cosmic history (Papovich et al. 2015).

In addition to these results based on the statistical correlation between the GC age–metallicity distribution and galaxy formation

and assembly, we also use the detailed distribution of GCs in age–metallicity space to reconstruct the merger tree of the Milky Way. This is done by comparison to the median properties of galaxies in the 25 Mpc EAGLE Recal-L025N0752 volume (Schaye et al. 2015) at a given redshift and metallicity of newly formed stars. We find that GC metallicity is the strongest indicator of the mass of its host galaxy at formation, with a secondary dependence on GC age. Using this technique, we identify the individual progenitors of the Milky Way that contributed GCs, as well as their stellar mass growth and metal enrichment histories over the age range spanned by their GCs. The results obtained this way are shown to be consistent with and to extend the previous observational constraints of the Milky Way's metal enrichment history (see Fig. 4). Using the number of GCs expected to be contributed by the accreted satellites, we estimate that ∼40 per cent of the Galactic GCs have an *ex situ* origin. Out of the 157 GCs in the Harris (1996, 2010 edition) catalogue, this corresponds to 60–70 GCs, with the remaining ∼90 having formed *in situ*.

Fig. 6 summarizes many of the results presented in this paper by visualizing them in terms of the inferred merger tree of the Milky Way. This merger tree captures the following quantitative results from Section 4 (see specifically Tables 3 and 4), as well as the interpretation from Section 5.

(i) The main progenitor of the Milky Way experienced a total of $N_{\mathrm{br}} = 15 \pm 3$ mergers (or 'branches' of the merger tree), with $N_{\mathrm{br},z>2} = 9 \pm 2$ of these taking place at $z > 2$.

(ii) Out of these mergers, $N_{<1:100} = 8 \pm 2$ represent 'tiny' mergers with mass ratios <1:100, whereas the remainder represent minor (mass ratio 1:100–1:4) or possibly major (mass ratio >1:4) mergers. The Milky Way experienced no major mergers since $z \sim 4$.

(iii) The total number of progenitors is $N_{\mathrm{leaf}} = 24 \pm 10$ (or 'leaves' of the merger tree), implying that (after subtraction of the Milky Way's main progenitor and its direct mergers) about 8 progenitors must have merged with other progenitors prior to their accretion onto the Milky Way's main progenitor.

(iv) Through a combination of vigorous *in situ* star formation and satellite accretion, the main progenitor grows rapidly, attaining 10 per cent of its final mass at $z = 2.5$ and 50 per cent at $z = 1.2$.

(v) The GC age–metallicity distribution specifically indicates the presence of three satellite progenitors. Because these hosted most of the *ex situ* GCs, these are likely the most massive satellites to have been accreted by the Milky Way.

(vi) Out of the three identified satellites, the least massive one reaches a mass of $M_* \sim 4 \times 10^7 \, \mathrm{M_\odot}$ at $z = 3$. It likely corresponds to the Sagittarius dwarf galaxy, with a predicted stellar mass prior to accretion of a few $10^8 \, \mathrm{M_\odot}$, consistent with previous estimates. This low mass implies that it was accreted by the Milky Way through a tiny merger.

(vii) The remaining two identified satellites are indistinguishable on the satellite branch in the GC age–metallicity distribution, but (at least) two such progenitors are required to explain the large number of GCs on the satellite branch. They reach a mass of $M_* \sim 1 \times 10^9 \, \mathrm{M_\odot}$ at $z = 1.7$ and thus must be part of the ∼6 galaxies that are accreted at $z < 2$. Given their relatively high masses, these galaxies were accreted as minor mergers rather than tiny ones. One of these two massive satellite progenitors is suggested to have brought in the GCs historically associated with the Canis Major 'dwarf' (see footnote 15), with a mass of $M_* = 1–2 \times 10^9 \, \mathrm{M_\odot}$ at the time of accretion.

(viii) The presence of many (relatively metal-rich) GCs on the satellite branch unassociated with any known satellites predicts the
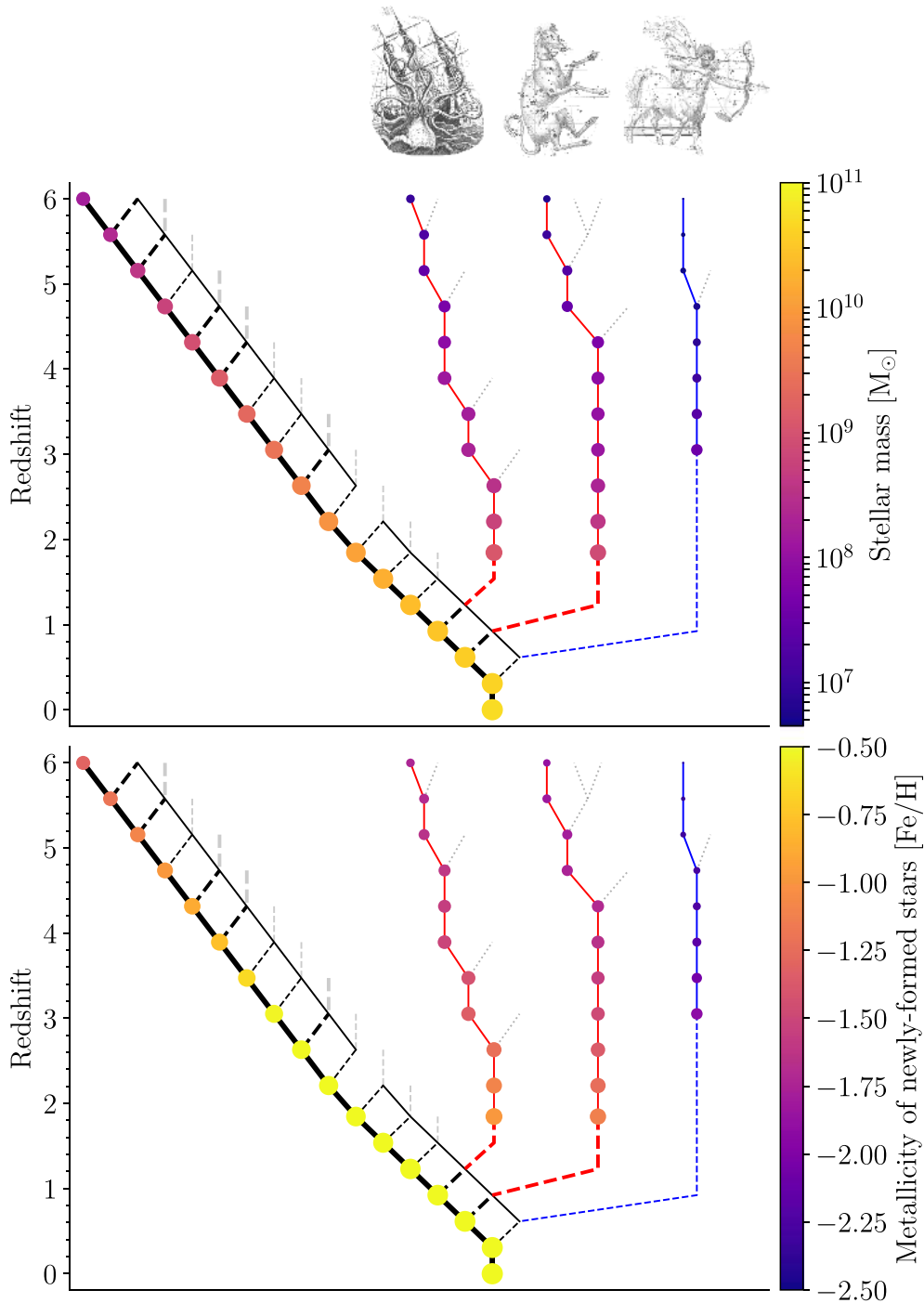
Figure 6. Galaxy merger tree of the Milky Way, inferred using the Galactic GC age–metallicity distribution, colour coded by galaxy stellar mass (top panel) and the metallicity of newly formed stars (bottom panel). This figure summarizes many of the results presented in this paper. The main progenitor is denoted by the thick black line, whereas the coloured lines indicate the identified (and likely most massive) satellites; i.e., red lines refer to Satellite 1 (left) and Satellite 2 (right), whereas the blue line shows Satellite 3. Dashed lines indicate mergers that are topologically robust, but have unknown timing within a given redshift interval. Thin lines mark tiny mergers (with mass ratio <1:100), whereas lines of intermediate thickness denote minor (or possibly major) mergers (with mass ratio >1:100). Light grey lines represent progenitors that are included to illustrate the inferred global statistics of the Milky Way's merger tree, but have no absolute meaning. These merger trees are consistent with the total number of mergers (N_{br}), the number of high-redshift mergers ($N_{br,z>2}$), the total number of progenitors (N_{leaf}), and the numbers of tiny and minor mergers ($N_{<1:100}$ and $N_{1:100-1:4}$) from Table 3, as well as with the identified progenitors, their connection to known satellites from Section 5.1, and their evolution from Table 4. Note that only progenitors with masses $M_* > 4.5 \times 10^6 \, M_\odot$ are included. From left to right, the three images along the top of the figure indicate the three identified dwarf galaxies Kraken, the progenitor contributing the 'Canis Major' GCs, and Sagittarius.

existence of a hitherto unknown progenitor that likely represents the most massive satellite ever to have been accreted by the Milky Way, with a mass of $M_* \sim 2 \times 10^9$ M$_\odot$ at the time of accretion. We name this enigmatic galaxy *Kraken* and propose it is responsible for the break in the density profile of the stellar halo at $R \sim 25$ kpc (e.g. Watkins et al. 2009; Sesar et al. 2011), which requires it to have been accreted between $z = 0.6$ and 1.3 (Deason et al. 2013) and implies that its tidal debris has since dispersed.

These results and predictions are highly suitable for observational tests using the 6D phase space information of the Galactic stellar halo and the GC population. With the arrival of *Gaia*, it is possible to perform a targeted search for the stars and GCs that are associated with the identified satellite progenitors of the Milky Way. For instance, Section 5.1 lists the GCs that may be associated with Kraken based on their ages and metallicities. This set of candidates can be pruned using their 3D positions and kinematics, thus providing the GCs that formed in Kraken with high confidence. More broadly, the statistical properties of the Milky Way's progenitors summarized above and in Fig. 6 are testable in future studies of stellar abundances and their phase-space information.[22]

Our constraints on the formation and assembly history of the Milky Way match and extend a broad range of previous findings from the literature, but also differ in some respects. For instance, the presented mass growth history and metal enrichment history of the Milky Way's main progenitor agree with (and add to) earlier results based on the field star population of the thick disc (Haywood et al. 2013; Snaith et al. 2014, 2015). Our conclusion that the Milky Way did not experience any major mergers since $z \sim 4$ sharpens the previous upper limit of having had no major mergers since $z \sim 2$ (Wyse 2001; Hammer et al. 2007; Stewart et al. 2008). Turning to the Milky Way's satellite progenitors, the mass range of the three identified, most massive accreted satellites ($M_* = 2 \times 10^8$–2×10^9 M$_\odot$) is consistent with the upper end of the satellite progenitor mass range of Milky Way-mass galaxies with relatively quiescent

assembly histories (Deason et al. 2016). The total number of 15 ± 3 mergers is consistent with previous estimates based on the structural properties of GCs (13–18 mergers, see Mackey & Gilmore 2004), even if the satellite masses are higher by a factor of several in our interpretation. This difference arises because we do not assume that all of their stellar mass is deposited into the stellar halo, but expect a significant fraction to be added to the Galactic disc and bulge. About half of the accreted satellites had masses too low to have been associated with GCs ($M_* \lesssim 2 \times 10^7$ M$_\odot$), implying that the remaining population spanning $M_* = 2 \times 10^7$–2×10^9 M$_\odot$ contributed the *ex situ* GC population of the Milky Way. These masses are considerably higher and span a narrower range than the previous estimate of Leaman et al. (2013), which results from their assumption that the entire old, metal-poor (halo) GC population formed *ex situ*. As discussed in Kruijssen et al. (2019), the E-MOSAICS simulations show that only about half of these GCs have an *ex situ* origin, and often formed in the (at that time still low-mass) precursors to the most massive accreted satellites. Finally, we combine these results with the dwarf galaxy nucleation fractions observed in the Fornax Cluster and predict that the Galactic GC population hosts $N_{\rm nucl} = 6 \pm 1$ former nuclear clusters, which are likely to exhibit a spread in [Fe/H].

This work demonstrates that the Galactic GC population provides detailed insight into the formation and assembly history of the Milky Way. After a rapid phase of *in situ* growth and copious dwarf galaxy accretion that lasted until $z = 2$–4, the Milky Way evolved quiescently, accreting satellites of low to intermediate masses through tiny and minor mergers. The detailed information encoded in the GC age–metallicity distribution enables us to identify several of the most massive progenitors of the Milky Way and constrain their mass growth and metal enrichment histories, including the Sagittarius dwarf, the galaxy contributing the 'Canis Major' GCs, and a newly postulated, most massive accreted satellite of the Milky Way, which we name *Kraken*. While the GC age–metallicity distribution is unlikely to provide meaningful insight into the formation of galaxies outside the virial radius of the Milky Way due to the poor precision of absolute GC ages at such distances, it may be possible to identify the youngest GCs in other galaxies within (or just outside) the Local Group and use these to infer the properties of their satellite progenitors. In addition, we expect GC-related observables other than their ages to facilitate comparable analyses of more distant galaxies. Examples of specific observables of interest are the spatial distribution of GCs, their metallicity distribution, their kinematics, and their association with stellar streams. In future work, we will explore these and other connections between GC populations and their host galaxies' formation and assembly histories.

ACKNOWLEDGEMENTS

REFERENCES

Abadi M. G., Navarro J. F., Steinmetz M., Eke V. R., 2003, ApJ, 597, 21
Adamo A., Bastian N., 2018, in Stahler S., Astrophysics and Space Science Library,, ed., Vol. 424, The Birth of Star Clusters, Springer, Cham. p. 91
Adamo A., Kruijssen J. M. D., Bastian N., Silva-Villa E., Ryon J., 2015, MNRAS, 452, 246
Allen C., Moreno E., Pichardo B., 2006, ApJ, 652, 1150
Amorisco N. C., 2017, MNRAS, 464, 2882
Amorisco N. C., Evans N. W., van de Ven G., 2014, Nature, 507, 335
Annibali F. et al., 2018, MNRAS, 476, 1942
Astropy Collaboration, 2013, A&A, 558, A33
Bahé Y. M. et al., 2016, MNRAS, 456, 1115
Bastian N., 2008, MNRAS, 390, 759
Bastian N., Lardo C., 2018, ARA&A, preprint (arXiv:1712.01286)
Beasley M. A., Trujillo I., Leaman R., Montes M., 2018, Nature, 555, 483
Behroozi P. S., Wechsler R. H., Conroy C., 2013, ApJ, 770, 57
Bekki K., Freeman K. C., 2003, MNRAS, 346, L11
Bellazzini M., Ferraro F. R., Ibata R., 2002, AJ, 124, 915
Bellazzini M., Ferraro F. R., Ibata R., 2003, AJ, 125, 188
Belokurov V. et al., 2006, ApJ, 642, L137
Belokurov V., 2013, New A Rev., 57, 100
Belokurov V., Erkal D., Evans N. W., Koposov S. E., Deason A. J., 2018, MNRAS, 478, 611
Blakeslee J. P., 1997, ApJ, 481, L59
Bland-Hawthorn J., Gerhard O., 2016, ARA&A, 54, 529
Boggs P. T., Rogers J. E., 1990, Contemporary Mathematics, 112, 183
Booth C. M., Schaye J., 2009, MNRAS, 398, 53
Carballo-Bello J. A., Martínez-Delgado D., Navarrete C., Catelan M., Muñoz R. R., Antoja T., Sollima A., 2018, MNRAS, 474, 683
Carraro G., 2009, AJ, 137, 3809
Carraro G., Zinn R., Moni Bidin C., 2007, A&A, 466, 181
Carretta E., 2015, ApJ, 810, 148
Carretta E., Gratton R. G., 1997, A&AS, 121, 95
Carretta E., Bragaglia A., Gratton R., D'Orazi V., Lucatello S., 2009, A&A, 508, 695
Carretta E. et al., 2010, ApJ, 714, L7

Catelan M., Borissova J., Ferraro F. R., Corwin T. M., Smith H. A., Kurtev R., 2002, AJ, 124, 364
Chantereau W., Charbonnel C., Meynet G., 2016, A&A, 592, A111
Correa C. A., Wyithe J. S. B., Schaye J., Duffy A. R., 2015, MNRAS, 452, 1217
Côté P., Marzke R. O., West M. J., 1998, ApJ, 501, 554
Côté P., Marzke R. O., West M. J., Minniti D., 2000, ApJ, 533, 869
Crain R. A. et al., 2015, MNRAS, 450, 1937
Crain R. A. et al., 2017, MNRAS, 464, 4204
Crnojević D. et al., 2016, ApJ, 823, 19
Dalla Vecchia C., Schaye J., 2012, MNRAS, 426, 140
De Angeli F., Piotto G., Cassisi S., Busso G., Recio-Blanco A., Salaris M., Aparicio A., Rosenberg A., 2005, AJ, 130, 116
de Boer T. J. L., Belokurov V., Koposov S. E., 2018, MNRAS, 473, 647
Deason A. J., Belokurov V., Evans N. W., Johnston K. V., 2013, ApJ, 763, 113
Deason A., Wetzel A., Garrison-Kimmel S., 2014, ApJ, 794, 115
Deason A. J., Belokurov V., Weisz D. R., 2015, MNRAS, 448, L77
Deason A. J., Mao Y.-Y., Wechsler R. H., 2016, ApJ, 821, 5
Deason A. J., Belokurov V., Koposov S. E., Lancaster L., 2018a, ApJ, 861, L1
Deason A. J., Belokurov V., Koposov S. E., 2018b, MNRAS, 473, 2428
Dinescu D. I., Girard T. M., van Altena W. F., 1999, AJ, 117, 1792
Dotter A., 2013, Mem. Soc. Astron. Italiana, 84, 97
Dotter A., Sarajedini A., Yang S.-C., 2008, AJ, 136, 1407
Dotter A. et al., 2010, ApJ, 708, 698
Dotter A., Sarajedini A., Anderson J., 2011, ApJ, 738, 74
Durrell P. R. et al., 2014, ApJ, 794, 103
Eggen O. J., Lynden-Bell D., Sandage A. R., 1962, ApJ, 136, 748
Forbes D. A., Bridges T., 2010, MNRAS, 404, 1203
Forbes D. A., Brodie J. P., Grillmair C. J., 1997, AJ, 113, 1652
Forbes D. A., Strader J., Brodie J. P., 2004, AJ, 127, 3394
Forbes D. A., Pastorello N., Romanowsky A. J., Usher C., Brodie J. P., Strader J., 2015, MNRAS, 452, 1045
Forbes D. A. et al., 2018, Proc. R. Soc. A, 474, 20170616
Freeman K., Bland-Hawthorn J., 2002, ARA&A, 40, 487
Freeman P., Rosolowsky E., Kruijssen J. M. D., Bastian N., Adamo A., 2017, MNRAS, 468, 1769
Furlong M. et al., 2015, MNRAS, 450, 4486
Furlong M. et al., 2017, MNRAS, 465, 722
Gaia Collaboration, 2016a, A&A, 595, A1
Gaia Collaboration, 2016b, A&A, 595, A2
Gaia Collaboration, 2018a, A&A, 616, A12
Gaia Collaboration, 2018b, A&A, 616, A1
Goddard Q. E., Bastian N., Kennicutt R. C., 2010, MNRAS, 405, 857
Grillmair C. J., 2009, ApJ, 693, 1118
Haardt F., Madau P., 2001, in Neumann D. M., Tran J. T. V., eds, XXXVIth Recontres de Moriond, Clusters of Galaxies and the High Redshift Universe Observed in X-rays,
Hammer F., Puech M., Chemin L., Flores H., Lehnert M. D., 2007, ApJ, 662, 322
Harris W. E., 1996, AJ, 112, 1487
Harris W. E., Blakeslee J. P., Harris G. L. H., 2017, ApJ, 836, 67
Haywood M., Di Matteo P., Lehnert M. D., Katz D., Gómez A., 2013, A&A, 560, A109
Henry T. J., McCarthy Jr. D. W., 1993, AJ, 106, 773
Hunter J. D., 2007, Computing in Science & Engineering, 9, 90
Ibata R. A., Gilmore G., Irwin M. J., 1994, Nature, 370, 194
Johnson L. C. et al., 2016, ApJ, 827, 33
Jones E. et al., 2001, SciPy: Open source scientific tools for Python, http://www.scipy.org/
Jordán A. et al., 2007, ApJS, 171, 101
Kraft R. P., Ivans I. I., 2003, PASP, 115, 143
Kruijssen J. M. D., 2012, MNRAS, 426, 3008
Kruijssen J. M. D., 2014, Class. Quantum Gravity, 31, 244006
Kruijssen J. M. D., Mieske S., 2009, A&A, 500, 785
Kruijssen J. M. D., Pelupessy F. I., Lamers H. J. G. L. M., Portegies Zwart S. F., Icke V., 2011, MNRAS, 414, 1339

Kruijssen J. M. D., Pelupessy F. I., Lamers H. J. G. L. M., Portegies Zwart S. F., Bastian N., Icke V., 2012, MNRAS, 421, 1927

Kruijssen J. M. D., Pfeffer J. L., Crain R. A., Bastian N., 2019, MNRAS, preprint (arXiv:1904.04261)

Lagos C. d. P. et al., 2015, MNRAS, 452, 3815

Lamers H. J. G. L. M., Gieles M., Bastian N., Baumgardt H., Kharchenko N. V., Portegies Zwart S., 2005, A&A, 441, 117

Law D. R., Majewski S. R., 2010, ApJ, 718, 1128

Layden A. C., Sarajedini A., 2000, AJ, 119, 1760

Leaman R., VandenBerg D. A., Mendel J. T., 2013, MNRAS, 436, 122

Mackereth J. T., Crain R. A., Schiavon R. P., Schaye J., Theuns T., Schaller M., 2018, MNRAS, 477, 5072

Mackey A. D., Gilmore G. F., 2004, MNRAS, 355, 504

Majewski S. R., Skrutskie M. F., Weinberg M. D., Ostheimer J. C., 2003, ApJ, 599, 1082

Malkov O. Y., 2007, MNRAS, 382, 1073

Marín-Franch A. et al., 2009, ApJ, 694, 1498

Martin N. F., Ibata R. A., Bellazzini M., Irwin M. J., Lewis G. F., Dehnen W., 2004, MNRAS, 348, 12

Martínez-Delgado D., Butler D. J., Rix H.-W., Franco V. I., Peñarrubia J., Alfaro E. J., Dinescu D. I., 2005, ApJ, 633, 205

McConnachie A. W. et al., 2009, Nature, 461, 66

McLaughlin D. E., van der Marel R. P., 2005, ApJS, 161, 304

Messa M. et al., 2018, MNRAS, 477, 1683

Meza A., Navarro J. F., Abadi M. G., Steinmetz M., 2005, MNRAS, 359, 93

Miholics M., Kruijssen J. M. D., Sills A., 2017, MNRAS, 470, 1421

Moster B. P., Naab T., White S. D. M., 2013, MNRAS, 428, 3121

Muñoz R. P. et al., 2015, ApJ, 813, L15

Myeong G. C., Evans N. W., Belokurov V., Sanders J. L., Koposov S. E., 2018, ApJ, 863, L28

Nakanishi H., Sofue Y., 2016, PASJ, 68, 5

Niederste-Ostholt M., Belokurov V., Evans N. W., Peñarrubia J., 2010, ApJ, 712, 516

Niederste-Ostholt M., Belokurov V., Evans N. W., 2012, MNRAS, 422, 207

Oppenheimer B. D. et al., 2016, MNRAS, 460, 2157

Ordenes-Briceño Y. et al., 2018, ApJ, 860, 4

Oser L., Ostriker J. P., Naab T., Johansson P. H., Burkert A., 2010, ApJ, 725, 2312

Papovich C. et al., 2015, ApJ, 803, 26

Peñarrubia J. et al., 2005, ApJ, 626, 128

Pfeffer J., Griffen B. F., Baumgardt H., Hilker M., 2014, MNRAS, 444, 3670

Pfeffer J., Kruijssen J. M. D., Crain R. A., Bastian N., 2018, MNRAS, 475, 4309

Pillepich A. et al., 2014, MNRAS, 444, 237

Planck CollaborationI, 2014, A&A, 571, A1

Rahmati A., Schaye J., Bower R. G., Crain R. A., Furlong M., Schaller M., Theuns T., 2015, MNRAS, 452, 2034

Reina-Campos M., Kruijssen J. M. D., 2017, MNRAS, 469, 1282

Reina-Campos M., Kruijssen J. M. D., Pfeffer J., Crain R. A., Bastian N., 2018a, MNRAS, preprint (arXiv:e-print)

Reina-Campos M., Kruijssen J. M. D., Pfeffer J., Bastian N., Crain R. A., 2018b, MNRAS, preprint (arXiv:e-print)

Rosas-Guevara Y. M. et al., 2015, MNRAS, 454, 1038

Salaris M., Weiss A., 1998, A&A, 335, 943

Salaris M., Weiss A., Ferguson J. W., Fusilier D. J., 2006, ApJ, 645, 1131

Sales L. V., Navarro J. F., Abadi M. G., Steinmetz M., 2007, MNRAS, 379, 1464

Schaye J., 2004, ApJ, 609, 667

Schaye J., Dalla Vecchia C., 2008, MNRAS, 383, 1210

Schaye J. et al., 2015, MNRAS, 446, 521

Searle L., Zinn R., 1978, ApJ, 225, 357

Sellwood J. A., Binney J. J., 2002, MNRAS, 336, 785

Sesar B., Jurić M., Ivezić Ž., 2011, ApJ, 731, 4

Shen J., Rich R. M., Kormendy J., Howard C. D., De Propris R., Kunder A., 2010, ApJ, 720, L72

Siegel M. H. et al., 2007, ApJ, 667, L57

Snaith O. N., Haywood M., Di Matteo P., Lehnert M. D., Combes F., Katz D., Gómez A., 2014, ApJ, 781, L31

Snaith O., Haywood M., Di Matteo P., Lehnert M. D., Combes F., Katz D., Gómez A., 2015, A&A, 578, A87

Sofue Y., 2015, PASJ, 67, 75

Sohn S. T., Watkins L. L., Fardal M. A., van der Marel R. P., Deason A. J., Besla G., Bellini A., 2018, ApJ, 862, 52

Spitler L. R., Forbes D. A., 2009, MNRAS, 392, L1

Springel V., 2005, MNRAS, 364, 1105

Springel V., Di Matteo T., Hernquist L., 2005, MNRAS, 361, 776

Stewart K. R., Bullock J. S., Wechsler R. H., Maller A. H., Zentner A. R., 2008, ApJ, 683, 597

Strader J. et al., 2011, ApJS, 197, 33

Trayford J. W. et al., 2015, MNRAS, 452, 2879

Usher C., Pfeffer J., Bastian N., Kruijssen J. M. D., Crain R. A., Reina-Campos M., 2018, MNRAS, 480, 3279

van der Walt S., Colbert S. C., Varoquaux G., 2011, Computing in Science & Engineering, 13, 22

VandenBerg D. A., Brogaard K., Leaman R., Casagrande L., 2013, ApJ, 775, 134

VandenBerg D. A., Bergbusch P. A., Ferguson J. W., Edvardsson B., 2014, ApJ, 794, 72

VandenBerg D. A., Denissenkov P. A., Catelan M., 2016, ApJ, 827, 2

Wagner-Kaiser R. et al., 2017, MNRAS, 471, 3347

Ward J. L., Kruijssen J. M. D., 2018, MNRAS, 475, 5659

Watkins L. L. et al., 2009, MNRAS, 398, 1757

White S. D. M., Frenk C. S., 1991, ApJ, 379, 52

White S. D. M., Rees M. J., 1978, MNRAS, 183, 341

Wiersma R. P. C., Schaye J., Smith B. D., 2009a, MNRAS, 393, 99

Wiersma R. P. C., Schaye J., Theuns T., Dalla Vecchia C., Tornatore L., 2009b, MNRAS, 399, 574

Wyse R. F. G., 2001, in Funes J. G., Corsini E. M., eds, ASP Conf. Ser. Vol. 230, Galaxy Disks and Disk Galaxies. Astron Soc. Pac., San Francisco, p. 71

APPENDIX A: OBSERVED PROPERTIES OF THE GC POPULATION IN THE MILKY WAY

We list the observed properties of the Galactic GC population in Table A1. This includes the absolute V-band magnitudes from Harris (1996, 2010 edition), cluster masses assuming $M_{V,\odot} = 4.83$ and $M/L_V = 2\,\mathrm{M_\odot L_\odot^{-1}}$ (e.g. McLaughlin & van der Marel 2005; Kruijssen & Mieske 2009; Strader et al. 2011), and the ages τ and metallicities [Fe/H] from three literature GC samples (Forbes & Bridges 2010; Dotter et al. 2010; Dotter et al. 2011; VandenBerg et al. 2013), as well as a combined sample, which takes the mean whenever multiple measurements are available per GC. For all samples, the maximum age is set to $\tau_{\max} = \tau_H - 0.18$ Gyr, which corresponds to $z = 20$. The individual age uncertainties are listed for each GC, but we assume a universal metallicity uncertainty of $\sigma([Fe/H]) = 0.1$ dex. For the VandenBerg et al. (2013) sample, the uncertainties include the statistical uncertainty listed in their paper, as well as an additional uncertainty of 1 Gyr to account for uncertainties in distance and chemical abundances. The error bars quoted for the other samples already include these sources of uncertainty. See Section 3 for further discussion.

Table A1. Observed properties of 96 Galactic GCs based on three main GC age–metallicity samples from the literature. From left to right, the columns show the following: GC name; absolute *V*-band magnitude M_V from Harris (1996, 2010 edition), implied mass M assuming $M_{V,\odot} = 4.83$, and $M/L_V = 2$; ages τ and metallicities [Fe/H] from the Forbes & Bridges (2010), Dotter et al. (2010, 2011), and VandenBerg et al. (2013) samples; mean age across all three samples $\overline{\tau}$; mean metallicity across all three samples $\overline{[\text{Fe/H}]}$.

Name	M_V [mag]	$\log M$ [M$_\odot$]	Forbes & Bridges (2010) τ [Gyr]	[Fe/H]	Dotter et al. (2010, 2011) τ [Gyr]	[Fe/H]	VandenBerg et al. (2013) τ [Gyr]	[Fe/H]	Mean $\overline{\tau}$ [Gyr]	$\overline{[\text{Fe/H}]}$
NGC 104	−9.42	6.00	13.06 ± 0.90	−0.78	12.75 ± 0.50	−0.70	11.75 ± 1.03	−0.76	12.52 ± 0.49	−0.75
NGC 288	−6.75	4.93	10.62 ± 0.51	−1.14	12.50 ± 0.50	−1.40	11.50 ± 1.07	−1.32	11.54 ± 0.43	−1.29
NGC 362	−8.43	5.61	10.37 ± 0.51	−1.09	11.50 ± 0.50	−1.30	10.75 ± 1.03	−1.30	10.87 ± 0.42	−1.23
NGC 1261	−7.80	5.35	10.24 ± 0.51	−1.08	11.50 ± 0.50	−1.35	10.75 ± 1.03	−1.27	10.83 ± 0.42	−1.23
NGC 1851	−8.33	5.57	9.98 ± 0.51	−1.03	–	–	11.00 ± 1.03	−1.18	10.49 ± 0.58	−1.10
NGC 1904	−7.86	5.38	11.14 ± 0.90	−1.37	–	–	–	–	11.14 ± 0.90	−1.37
NGC 2298	−6.31	4.76	12.67 ± 0.64	−1.71	13.00 ± 1.00	−1.90	–	–	12.84 ± 0.59	−1.80
NGC 2419	−9.42	6.00	12.30 ± 1.00	−2.14	13.00 ± 1.00	−2.00	–	–	12.65 ± 0.71	−2.07
NGC 2808	−9.39	5.99	10.80 ± 0.38	−1.11	–	–	11.00 ± 1.07	−1.18	10.90 ± 0.57	−1.14
NGC 3201	−7.45	5.21	10.24 ± 0.38	−1.24	12.00 ± 0.75	−1.50	11.50 ± 1.07	−1.51	11.25 ± 0.45	−1.42
NGC 4147	−6.17	4.70	11.39 ± 0.51	−1.50	12.75 ± 0.75	−1.70	12.25 ± 1.03	−1.78	12.13 ± 0.46	−1.66
NGC 4372	−7.79	5.35	12.54 ± 0.90	−1.88	–	–	–	–	12.54 ± 0.90	−1.88
NGC 4590	−7.37	5.18	11.52 ± 0.51	−2.00	13.00 ± 1.00	−2.30	12.00 ± 1.03	−2.27	12.17 ± 0.51	−2.19
NGC 4833	−8.17	5.50	12.54 ± 0.64	−1.71	13.00 ± 1.25	−2.30	12.50 ± 1.12	−1.89	12.68 ± 0.60	−1.97
NGC 5024	−8.71	5.72	12.67 ± 0.64	−1.86	13.25 ± 0.50	−2.00	12.25 ± 1.03	−2.06	12.72 ± 0.44	−1.97
NGC 5053	−6.76	4.94	12.29 ± 0.51	−1.98	13.50 ± 0.75	−2.40	12.25 ± 1.07	−2.30	12.68 ± 0.47	−2.23
NGC 5139	−10.26	6.34	11.52 ± 0.64	−1.35	–	–	–	–	11.52 ± 0.64	−1.35
NGC 5272	−8.88	5.79	11.39 ± 0.51	−1.34	12.50 ± 0.50	−1.60	11.75 ± 1.03	−1.50	11.88 ± 0.42	−1.48
NGC 5286	−8.74	5.73	12.54 ± 0.51	−1.41	13.00 ± 1.00	−1.70	12.50 ± 1.07	−1.70	12.68 ± 0.52	−1.60
NGC 5466	−6.98	5.03	13.57 ± 0.64	−2.20	13.00 ± 0.75	−2.10	12.50 ± 1.03	−2.31	13.02 ± 0.48	−2.20
NGC 5634	−7.69	5.31	11.84 ± 0.51	−1.94	–	–	–	–	11.84 ± 0.51	−1.94
NGC 5694	−7.83	5.37	13.44 ± 0.90	−1.74	–	–	–	–	13.44 ± 0.90	−1.74
NGC 5824	−8.85	5.77	12.80 ± 0.90	−1.60	–	–	–	–	12.80 ± 0.90	−1.60
NGC 5897	−7.23	5.13	12.30 ± 1.20	−1.73	–	–	–	–	12.30 ± 1.20	−1.73
NGC 5904	−8.81	5.76	10.62 ± 0.38	−1.12	12.25 ± 0.75	−1.30	11.50 ± 1.03	−1.33	11.46 ± 0.44	−1.25
NGC 5927	−7.81	5.36	12.67 ± 0.90	−0.64	12.25 ± 0.75	−0.50	10.75 ± 1.07	−0.29	11.89 ± 0.53	−0.48
NGC 5946	−7.18	5.11	11.39 ± 0.90	−1.22	–	–	–	–	11.39 ± 0.90	−1.22
NGC 5986	−8.44	5.61	12.16 ± 0.51	−1.35	13.25 ± 1.00	−1.60	12.25 ± 1.25	−1.63	12.55 ± 0.56	−1.53
NGC 6093	−8.23	5.53	12.54 ± 0.51	−1.47	13.50 ± 1.00	−1.70	–	–	13.02 ± 0.56	−1.58
NGC 6101	−6.94	5.01	12.54 ± 0.51	−1.76	13.00 ± 1.00	−1.80	12.25 ± 1.12	−1.98	12.60 ± 0.53	−1.85
NGC 6121	−7.19	5.11	12.54 ± 0.64	−1.05	12.50 ± 0.50	−1.20	11.50 ± 1.07	−1.18	12.18 ± 0.45	−1.14
NGC 6144	−6.85	4.97	13.82 ± 0.64	−1.56	13.50 ± 1.00	−1.80	12.75 ± 1.12	−1.82	13.36 ± 0.54	−1.73
NGC 6171	−7.12	5.08	13.95 ± 0.77	−0.95	12.75 ± 0.75	−1.00	12.00 ± 1.25	−1.03	12.90 ± 0.55	−0.99
NGC 6205	−8.55	5.65	11.65 ± 0.51	−1.33	13.00 ± 0.50	−1.60	12.00 ± 1.07	−1.58	12.22 ± 0.43	−1.50
NGC 6218	−7.31	5.16	12.67 ± 0.38	−1.14	13.25 ± 0.75	−1.30	13.00 ± 1.12	−1.33	12.97 ± 0.47	−1.26
NGC 6235	−6.29	4.75	11.39 ± 0.90	−1.18	–	–	–	–	11.39 ± 0.90	−1.18
NGC 6254	−7.48	5.23	11.39 ± 0.51	−1.25	13.00 ± 1.25	−1.55	11.75 ± 1.07	−1.57	12.05 ± 0.57	−1.46
NGC 6266	−9.18	5.91	11.78 ± 0.90	−1.02	–	–	–	–	11.78 ± 0.90	−1.02
NGC 6273	−9.13	5.89	11.90 ± 0.90	−1.53	–	–	–	–	11.90 ± 0.90	−1.53
NGC 6284	−7.96	5.42	11.14 ± 0.90	−1.13	–	–	–	–	11.14 ± 0.90	−1.13
NGC 6287	−7.36	5.18	13.57 ± 0.90	−1.91	–	–	–	–	13.57 ± 0.90	−1.91
NGC 6304	−7.30	5.15	13.57 ± 1.02	−0.66	12.75 ± 0.75	−0.50	11.25 ± 1.07	−0.37	12.52 ± 0.55	−0.51
NGC 6341	−8.21	5.52	13.18 ± 0.51	−2.16	13.25 ± 1.00	−2.40	12.75 ± 1.03	−2.35	13.06 ± 0.51	−2.30
NGC 6342	−6.42	4.80	12.03 ± 0.90	−0.69	–	–	–	–	12.03 ± 0.90	−0.69
NGC 6352	−6.47	4.82	12.67 ± 0.90	−0.70	13.00 ± 0.50	−0.80	10.75 ± 1.07	−0.62	12.14 ± 0.49	−0.71
NGC 6362	−6.95	5.01	13.57 ± 0.64	−0.99	12.50 ± 0.50	−1.10	12.50 ± 1.03	−1.07	12.86 ± 0.44	−1.05
NGC 6366	−5.74	4.53	13.31 ± 1.66	−0.73	12.00 ± 0.75	−0.70	11.00 ± 1.12	−0.59	12.10 ± 0.71	−0.67
NGC 6388	−9.41	6.00	12.03 ± 1.02	−0.77	–	–	–	–	12.03 ± 1.02	−0.77
NGC 6397	−6.64	4.89	12.67 ± 0.51	−1.76	13.50 ± 0.50	−2.10	13.00 ± 1.03	−1.99	13.06 ± 0.42	−1.95
NGC 6426	−6.67	4.90	12.90 ± 1.00	−2.11	13.00 ± 1.50	−2.20	–	–	12.95 ± 0.90	−2.16
NGC 6441	−9.63	6.09	11.26 ± 0.90	−0.60	–	–	–	–	11.26 ± 0.90	−0.60
NGC 6496	−7.20	5.11	12.42 ± 0.90	−0.70	12.00 ± 0.75	−0.50	10.75 ± 1.07	−0.46	11.72 ± 0.53	−0.55
NGC 6535	−4.75	4.13	10.50 ± 1.15	−1.51	13.25 ± 1.00	−1.90	12.75 ± 1.12	−1.79	12.17 ± 0.63	−1.73
NGC 6541	−8.52	5.64	12.93 ± 0.51	−1.53	13.25 ± 1.00	−1.90	12.50 ± 1.12	−1.82	12.89 ± 0.53	−1.75
NGC 6544	−6.94	5.01	10.37 ± 0.90	−1.20	–	–	–	–	10.37 ± 0.90	−1.20
NGC 6584	−7.69	5.31	11.26 ± 0.38	−1.30	12.25 ± 0.75	−1.40	11.75 ± 1.12	−1.50	11.75 ± 0.47	−1.40

Table A1. *continued.*

Name	M_V [mag]	$\log M$ [M$_\odot$]	Forbes & Bridges (2010) τ [Gyr]	[Fe/H]	Dotter et al. (2010, 2011) τ [Gyr]	[Fe/H]	VandenBerg et al. (2013) τ [Gyr]	[Fe/H]	Mean $\overline{\tau}$ [Gyr]	$\overline{\text{[Fe/H]}}$
NGC 6624	−7.49	5.23	12.54 ± 0.90	−0.70	13.00 ± 0.75	−0.50	11.25 ± 1.12	−0.42	12.26 ± 0.54	−0.54
NGC 6637	−7.64	5.29	13.06 ± 0.90	−0.78	12.50 ± 0.75	−0.70	11.00 ± 1.07	−0.59	12.19 ± 0.53	−0.69
NGC 6652	−6.66	4.90	12.93 ± 0.77	−0.97	13.25 ± 0.50	−0.75	11.25 ± 1.03	−0.76	12.48 ± 0.46	−0.83
NGC 6656	−8.50	5.63	12.67 ± 0.64	−1.49	–	–	–	–	12.67 ± 0.64	−1.49
NGC 6681	−7.12	5.08	12.80 ± 0.51	−1.35	13.00 ± 0.75	−1.50	12.50 ± 1.12	−1.70	12.77 ± 0.48	−1.52
NGC 6712	−7.50	5.23	10.40 ± 1.40	−0.94	–	–	–	–	10.40 ± 1.40	−0.94
NGC 6715	−9.98	6.23	10.75 ± 0.38	−1.25	–	–	11.75 ± 1.12	−1.44	11.25 ± 0.59	−1.34
NGC 6717	−5.66	4.50	13.18 ± 0.64	−1.09	13.00 ± 0.75	−1.10	12.50 ± 1.12	−1.26	12.89 ± 0.59	−1.15
NGC 6723	−7.83	5.37	13.06 ± 0.64	−0.96	12.75 ± 0.50	−1.00	12.50 ± 1.03	−1.10	12.77 ± 0.44	−1.02
NGC 6752	−7.73	5.33	11.78 ± 0.51	−1.24	12.50 ± 0.75	−1.50	12.50 ± 1.03	−1.55	12.26 ± 0.46	−1.43
NGC 6779	−7.41	5.20	13.70 ± 0.64	−2.00	13.50 ± 1.00	−2.20	12.75 ± 1.12	−2.00	13.32 ± 0.54	−2.07
NGC 6809	−7.57	5.26	12.29 ± 0.51	−1.54	13.50 ± 1.00	−1.80	13.00 ± 1.03	−1.93	12.93 ± 0.51	−1.76
NGC 6838	−5.61	4.48	13.70 ± 1.02	−0.73	12.50 ± 0.75	−0.70	11.00 ± 1.07	−0.82	12.40 ± 0.55	−0.75
NGC 6864	−8.57	5.66	9.98 ± 0.51	−1.03	–	–	–	–	9.98 ± 0.51	−1.03
NGC 6934	−7.45	5.21	11.14 ± 0.51	−1.32	12.00 ± 0.75	−1.55	11.75 ± 1.03	−1.56	11.63 ± 0.46	−1.48
NGC 6981	−7.04	5.05	10.88 ± 0.26	−1.21	12.75 ± 0.75	−1.50	11.50 ± 1.03	−1.48	11.71 ± 0.43	−1.40
NGC 7006	−7.67	5.30	–	–	12.25 ± 0.75	−1.50	–	–	12.25 ± 0.75	−1.50
NGC 7078	−9.19	5.91	12.93 ± 0.51	−2.02	13.25 ± 1.00	−2.40	12.75 ± 1.03	−2.33	12.98 ± 0.51	−2.25
NGC 7089	−9.03	5.85	11.78 ± 0.51	−1.31	12.50 ± 0.75	−1.60	11.75 ± 1.03	−1.66	12.01 ± 0.46	−1.52
NGC 7099	−7.45	5.21	12.93 ± 0.64	−1.92	13.25 ± 1.00	−2.40	13.00 ± 1.03	−2.33	13.06 ± 0.52	−2.22
NGC 7492	−5.81	4.56	12.00 ± 1.40	−1.41	–	–	–	–	12.00 ± 1.40	−1.41
Pal 1	−2.52	3.24	7.30 ± 1.15	−0.70	–	–	–	–	7.30 ± 1.15	−0.70
Pal 3	−5.69	4.51	9.70 ± 1.30	−1.39	11.30 ± 0.50	−1.50	–	–	10.50 ± 0.70	−1.44
Pal 4	−6.01	4.64	9.50 ± 1.40	−1.07	10.90 ± 0.50	−1.30	–	–	10.20 ± 0.84	−1.18
Pal 5	−5.17	4.30	9.80 ± 1.40	−1.24	12.00 ± 1.00	−1.40	–	–	10.90 ± 0.86	−1.32
Pal 12	−4.47	4.02	8.83 ± 1.12	−0.83	9.50 ± 0.75	−0.80	9.00 ± 1.07	−0.81	9.11 ± 0.57	−0.81
Pal 14	−4.80	4.15	10.50 ± 1.00	−1.36	10.50 ± 0.50	−1.50	–	–	10.50 ± 0.56	−1.43
Pal 15	−5.51	4.44	–	–	13.00 ± 1.50	−2.00	–	–	13.00 ± 1.50	−2.00
Terzan 7	−5.01	4.24	7.30 ± 0.51	−0.56	8.00 ± 0.75	−0.60	–	–	7.65 ± 0.45	−0.58
Terzan 8	−5.07	4.26	12.16 ± 0.51	−1.80	13.50 ± 0.50	−2.40	13.00 ± 1.07	−2.34	12.89 ± 0.43	−2.18
AM 1	−4.73	4.13	11.10 ± 1.00	−1.47	11.10 ± 0.50	−1.50	–	–	11.10 ± 0.56	−1.48
AM 4	−1.81	2.96	9.00 ± 0.50	−0.97	–	–	–	–	9.00 ± 0.50	−0.97
Arp 2	−5.29	4.35	10.88 ± 0.77	−1.45	13.00 ± 0.75	−1.80	12.00 ± 1.07	−1.74	11.96 ± 0.51	−1.66
E 3	−4.12	3.88	12.80 ± 1.41	−0.83	–	–	–	–	12.80 ± 1.41	−0.83
Eridanus	−5.13	4.29	8.90 ± 1.60	−1.20	10.50 ± 0.50	−1.30	–	–	9.70 ± 0.84	−1.25
IC4499	−7.32	5.16	–	–	12.00 ± 0.75	−1.60	–	–	12.00 ± 0.75	−1.60
Lynga 7	−6.60	4.87	14.46 ± 1.79	−0.64	12.50 ± 1.00	−0.60	–	–	13.48 ± 1.03	−0.62
Pyxis	−5.73	4.53	–	–	11.50 ± 1.00	−1.50	–	–	11.50 ± 1.00	−1.50
Rup 106	−6.35	4.77	10.20 ± 1.40	−1.49	11.50 ± 0.50	−1.50	–	–	10.85 ± 0.74	−1.50
Whiting 1	−2.46	3.22	6.50 ± 0.75	−0.65	–	–	–	–	6.50 ± 0.75	−0.65

This paper has been typeset from a TEX/LATEX file prepared by the author.